

Final report for AOARD grant FA2386-11-1-4010

“Mode locking of lasers with atomic layer graphene”

July 2012

Principal investigator: A/Prof. Tang Dingyuan
Division of Microelectronics
School of Electrical and Electronic Engineering
Nanyang Technological University, Singapore 639798

Email: edytang@ntu.edu.sg

Phone: 65-67904337

Funding level: US\$80,000
Grant period: January 2011- April 2012

Report Documentation Page				Form Approved OMB No. 0704-0188	
Public reporting burden for the collection of information is estimated to average 1 hour per response, including the time for reviewing instructions, searching existing data sources, gathering and maintaining the data needed, and completing and reviewing the collection of information. Send comments regarding this burden estimate or any other aspect of this collection of information, including suggestions for reducing this burden, to Washington Headquarters Services, Directorate for Information Operations and Reports, 1215 Jefferson Davis Highway, Suite 1204, Arlington VA 22202-4302. Respondents should be aware that notwithstanding any other provision of law, no person shall be subject to a penalty for failing to comply with a collection of information if it does not display a currently valid OMB control number.					
1. REPORT DATE 27 NOV 2012		2. REPORT TYPE Final		3. DATES COVERED 11-01-2011 to 19-04-2012	
4. TITLE AND SUBTITLE Mode Locking of Lasers with Atomic Layer Graphene				5a. CONTRACT NUMBER FA23861114010	
				5b. GRANT NUMBER	
				5c. PROGRAM ELEMENT NUMBER	
6. AUTHOR(S) Dingyuan Tang				5d. PROJECT NUMBER	
				5e. TASK NUMBER	
				5f. WORK UNIT NUMBER	
7. PERFORMING ORGANIZATION NAME(S) AND ADDRESS(ES) Nanyang Technological University,50 Nanyang Avenue,639798,Singapore,NA,NA				8. PERFORMING ORGANIZATION REPORT NUMBER N/A	
9. SPONSORING/MONITORING AGENCY NAME(S) AND ADDRESS(ES) AOARD, UNIT 45002, APO, AP, 96338-5002				10. SPONSOR/MONITOR'S ACRONYM(S) AOARD	
				11. SPONSOR/MONITOR'S REPORT NUMBER(S) AOARD-114010	
12. DISTRIBUTION/AVAILABILITY STATEMENT Approved for public release; distribution unlimited					
13. SUPPLEMENTARY NOTES					
14. ABSTRACT In this research project, Chemical Vapor Deposition (CVD) was used to fabricate high quality large size atomic layer graphene followed by experimental investigation of nonlinear optical saturable absorption properties; this investigation confirmed that atomic layer graphene can exhibit ultrafast, super broadband, polarization insensitive saturable absorption, which can be exploited for the passive mode locking of lasers of various operating wavelengths. Self-started mode locking of Erbium-, Ytterbium-, and Thulium-doped solid state fiber lasers operating at 1.55&#61549;m, 1.03&#61549;m, and 2014nm, respectively, was demonstrated. It was also observed that the longer the laser operating wavelength, the easier to achieve mode locking. Graphene derivatives were prepared using chemical functionalization to modify the graphene saturable absorption properties. Attempts to use graphene to mode lock a semiconductor laser operating at 770nm failed.					
15. SUBJECT TERMS Graphene, Mode Locked Lasers, Saturable Absorption					
16. SECURITY CLASSIFICATION OF:			17. LIMITATION OF ABSTRACT Same as Report (SAR)	18. NUMBER OF PAGES 49	19a. NAME OF RESPONSIBLE PERSON
a. REPORT unclassified	b. ABSTRACT unclassified	c. THIS PAGE unclassified			

Abstract: Large size atomic layer graphene was fabricated using the chemical vapor deposition (CVD) technique. The fabricated atomic layer graphene was characterized and its nonlinear optical saturable absorption property was experimentally measured. Based on the saturable absorption of the atomic layer graphene different forms of passive laser mode lockers were fabricated. These are the fiber pigtailed transmission type graphene saturable absorber, graphene saturable absorber mirror, and the graphene-polymer nanocomposite saturable thin-films. Using the graphene based saturable absorbers we have successfully demonstrated self-started passive mode locking of lasers with different operating wavelengths, ranging from 1 μ m to 2 μ m. The vector solitons operation of a graphene mode locked erbium fiber laser was experimentally investigated.

1. **Introduction**

For many applications, such as optical communications, optical range finder, remote sensing, high speed sampling, compact low cost wavelength tunable optical pulse sources are needed. Semiconductor lasers and fiber lasers have proven to be compact, inexpensive, and efficient sources of optical radiation. By employing the mode locking technique, high repetition rate ultrashort optical pulses can be formed in these lasers. Among the various mode-locking schemes of lasers, passive mode locking has been intensively investigated. Passive mode locking uses a saturable absorber in the laser cavity to force a laser to emit short optical pulses. It has the advantages of easy to implement, compact size and low cost. Combining with the intrinsically small size of the semiconductor lasers and fiber lasers, passively mode locked semiconductor lasers and fiber lasers fit particularly well for applications like optical communications, remote sensing etc. Conventionally, passive mode locking of semiconductor and fiber lasers is achieved with specially made saturable absorbers based on the single or multiple quantum well materials, known as the semiconductor saturable absorber mirrors (SESAMs). SESAMs are not only difficult to make, requiring special design and the clean room fabrication facilities, but also have the drawback of narrow operation band and low damage threshold. Because of the narrow operating bandwidth of SESAMs, lasers operating at different wavelengths need to use different SESAMs that are fabricated with different design, quantum well materials, and different fabrication

procedures. Hence, it is important to identify other saturable absorbers that can be universally used for the passive mode locking of different wavelength lasers, and in the meantime, the new saturable absorbers are easy to make and low cost.

Recent advances on the materials research have shown that the atomic layer graphene, a single layer of carbon atoms arranged in a honeycomb lattice, possesses a number of novel electronic and optical properties. Graphene is so far the only known stable 2-dimensional material in the world. Due to its special atomic structure, graphene has a number of unique electronic properties, such as zero energy bandgap, very large carrier mobility, and linear energy dispersion relation. Since it was first isolated in 2004, graphene has been extensively investigated as the next generation material for the nano-electronics applications. In addition, graphene also possesses unique optical properties, such as it has strong and nearly wavelength independent linear optical absorption. In view of graphene's energy band structure, we expect that graphene would have broad band saturable light absorption, and its saturable absorption property could be exploited for passive mode locking lasers.

2. Research objectives of the project

The objectives of the project were a) to fabricate large size atomic layer graphene and characterize its saturable absorption properties; b) based on the saturable absorption property of graphene to further fabricate either the transmission type or the reflection type of laser mode lockers; c) to use the fabricated laser mode lockers to passive mode lock semiconductor and/or fiber lasers; d) to use the modern material fabrication techniques to improve the performance of the graphene-based mode lockers.

3. Preparation of graphene samples and graphene mode lockers

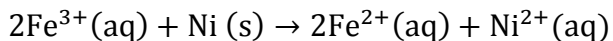
3.1 Atomic layer graphene fabrication and characterization

There are different approaches to synthesize atomic layer graphene. The first approach is the micromechanical exfoliation of graphite, which is also known as the "Scotch tape" or peel-off method. This approach gives the best samples in terms of electronic properties but the yield is quite low. The second method is epitaxial growth on

electrically insulating surfaces such as SiC. The third method is the chemical vapor deposition (CVD) on metal such as Ni and Cu. The CVD method can produce large area uniform graphene film, which can be used for make optoelectronic devices. The fourth approach is the creation of colloidal suspensions or liquid phase exfoliation, which includes the production of graphene and chemically modified graphene from colloidal suspensions made from graphite, derivatives of graphite (such as graphite oxide) and graphite intercalation compounds. This approach is both scalable, affording the possibility of high-volume production, and versatile in terms of being well-suited to chemical functionalization. In the project we used the CVD method to produce the few atomic layers graphene.

In a typical experiment, a SiO₂/Si substrate with 300 nm Ni film was loaded into a CVD chamber. Then, the Ni catalyst was activated at 700 °C in 100 sccm H₂ gas flow. The samples were heated up to 900 - 1000 °C inside a quartz tube under the flow of Ar/CH₄/H₂ mixture flow (Ar: CH₄: H₂: = 3: 1: 1) and reacted for 10 min. The Ni film and the carbon atoms can form a solid solution during the exposure of the Ni surface to a H₂ and CH₄ gas mixture. Finally, the system was allowed to rapidly cool down to room temperature at the rate of ~ 10 °C /s under the protection of Ar gas flow. Then carbon atoms precipitate as a graphene layer on the Ni surface upon cooling of the sample since the solubility of carbon in Ni is temperature-dependent. In this process, the graphene growth is likely due to the precipitation of graphite from carbon species within the metal thin film as observed for other transition metals, such as Ru, Ir and Pt.

An aqueous iron (III) chloride (FeCl₃) solution (~ 1M) was used as an oxidizing etchant to remove the Ni layer. The net ionic equation of the etching reaction can be written as



The process slowly etches the Ni layers while the sample floating on the FeCl₃ solution surface. Before the graphene film totally separated from the substrate, the sample was gently transferred into de-ionized (DI) water and let it floating on the water surface overnight to remove the attached ions. Then the graphene film was subsequently delaminated from Ni layers by dipping the samples into water using a floating off process

to obtain a freestanding film, as shown in Fig. 1. Before etching reaction, the dry Ni/SiO₂ substrate was cut into several sections so as to obtain graphene film with required size.

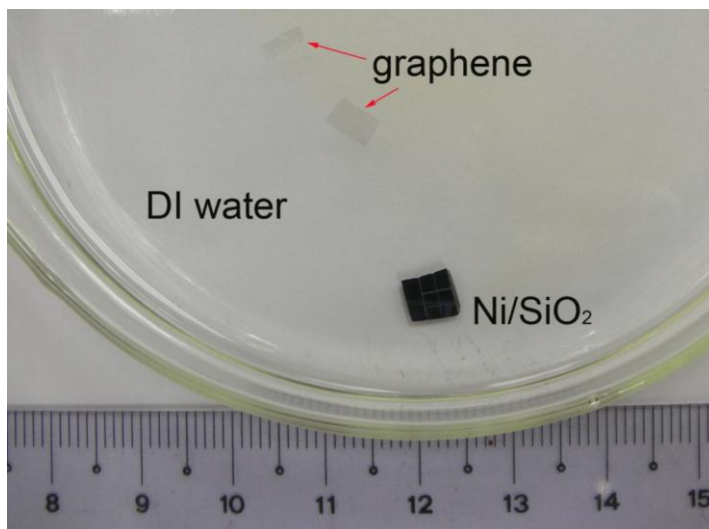


Figure 1. Photograph of graphene floating on DI water. The red arrows show two cut graphene films.

Atomic force microscopy (AFM, Dimension 3100 SPM) was used to study the morphologies and thickness of the as-produced and transferred graphene films. All the AFM images were obtained in tapping mode. Figure 2a and b show the typical topology and phase image of large size graphene film grown on Ni/SiO₂/Si substrate. Similar to the results reported by other groups, grain size and grain boundaries of polycrystalline Ni film are responsible for the observed morphologies. Phase image in Figure 2b shows that the graphene thin film is quite smooth within a grain. In this way, the growth of graphene on the surface of individual Ni grains resembles the growth of graphene on the surface of a single crystal substrate.

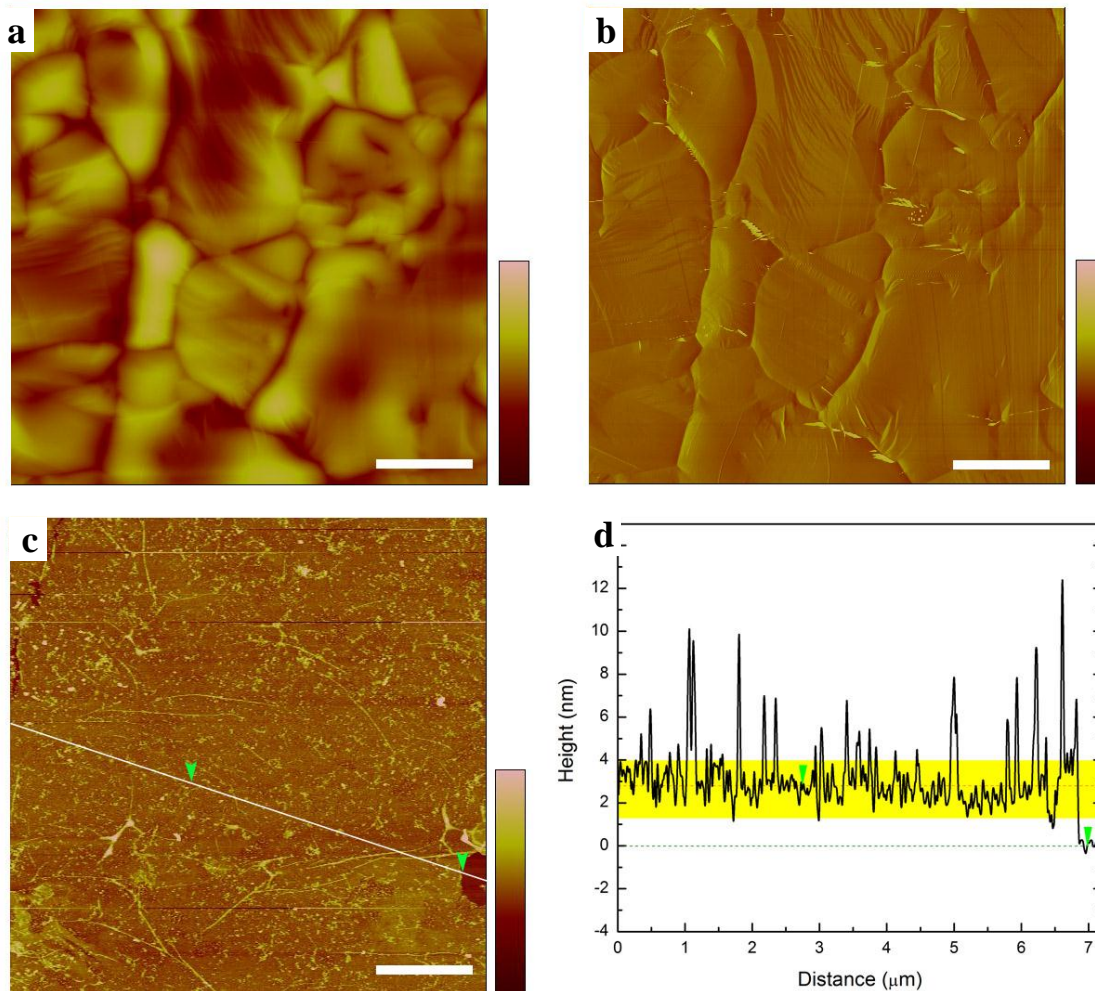


Figure 2. Atomic force microscopy (AFM) (a) topology and (b) phase image of large size graphene film grown on Ni/SiO₂/Si substrate. The scale bar in (a, b) is 2 μm and the vertical scale is 150 nm. (c) AFM topographic image and (d) height profile of graphene film transferred onto SiO₂ substrate. The scale bar in (c) is 2 μm and the vertical scale is 25 nm.

The graphene films transferred on Si substrate have quite different morphology characteristics from the as-produced one on Ni. The representative AFM topographic image and height profile of graphene film were shown in Figure 2c and d. There are several notable features: first, the large size graphene film is quite uniform in micron-meter size area; second, ripples with the length of micron-meter size and the height of several nano-meters are observed and the ripple structures are possibly caused by the different thermal expansion efficiencies between Ni and graphene and/or the uniaxial stress during sample transfer process; third, the height profile shows that the film

thickness were found to be between 1 to 4 nm corresponding to approximately 2-11 layers (with an average of about 2.8 ± 0.4 nm), the thinner part has a thickness of roughly 2 nm corresponding to 4 to 5 layers graphene and the thinnest part has a thickness of roughly 1 nm corresponding a monolayer or bilayer graphene.

To study the multilayer structure of graphene, transmission electron microscopy (TEM, JEOL 3010, 200 kV) was carried out. The same transfer method mentioned above was used to attach the graphene film onto lacey carbon-coated TEM grids. Figure 3a shows the typical TEM image of the as-prepared graphene thin film. The contrast shows some ripples and folded edges. The film is continuous and homogenous locally. The inset shows one folded edge of the graphene thin film, which confirms that the thickness correspond to 4-5 layers.

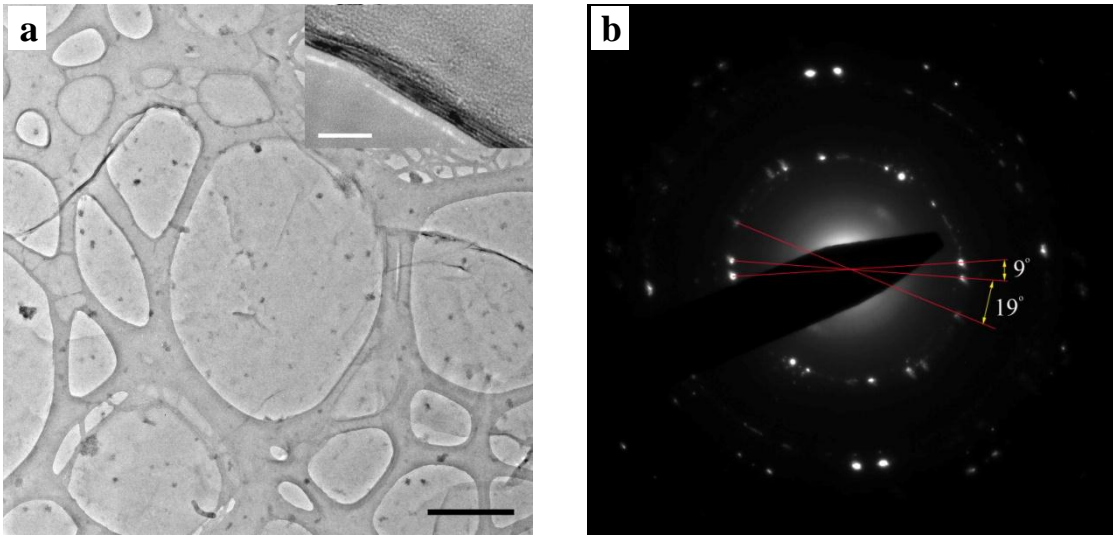


Figure 3. (a) Typical TEM image (scale bar: 500 nm, inset scale bar: 5 nm) and (b) corresponding SAED patterns of graphene layers.

Selective area electron diffraction (SAED) was used to inspect the quality of graphene film. Well defined diffraction spots (instead of ring patterns) are always observed while checking different regions of graphene film, which indicates high crystallinity. Figure 3b shows a representative diffraction pattern and it reveals a hexagonal pattern, confirming the three-fold symmetry of the arrangement of carbon atoms. Several sets of diffraction spots also with hexagonal symmetry, but with a misorientation, suggesting stacking disorder of graphene layers in multilayer regions.

Two rotation angles of 9° and 19° were observed from graphene layers. The stacking geometry of the as produced graphene is different from AB (Bernal) stacking in mechanical exfoliated graphene, similar to that of graphene grown on carbon terminated SiC surface.

The contrast spectroscopy in combination with the resonant Raman spectroscopy was used to identify the number of graphene layers. The Raman spectra were carried out with a WITEC CRM200 Raman system. The excitation source was a 532 nm laser (2.33 eV) with a laser power below 0.1 mW on the sample to avoid the laser-induced local heating. A 100X objective lens with a numerical aperture (NA) of 0.95 was used in the Raman experiments, and the spot size of 532 nm beam was estimated to be 500 nm. The spectra resolution of the Raman system is 1 cm^{-1} . The contrast between the graphene layers and the substrate, which makes the graphene visible, was generated from a reflection spectrum by using a normal white light source. To obtain the Raman images, a piezo-stage was used to move the sample with step size of 200 nm and Raman spectrum was recorded at every point. The stage movement and data acquisition were controlled using SCANCTRL SPECTROSCOPY PLUS software from WITec GmbH, Germany. Data analysis is done using WITEC PROJECT 1.88 software. As the basic component materials of fibre core and quartz are similar (SiO_2), we used the Raman and contrast spectra from graphene on quartz substrate as the reference. The contrast spectra $C(\lambda)$ are defined using the following equation,

$$C(\lambda) = \frac{R_0(\lambda) - R(\lambda)}{R_0(\lambda)}$$

Where $R_0(\lambda)$ is the reflection spectrum from substrate, and $R(\lambda)$ is the reflection spectrum from graphene sheets. It was found that the contrast value changes almost linearly with the number of graphene layers for thin graphene sheets. The contrast values are found to be around $M \times (-0.068)$ for M layers graphene on quartz substrate, i.e., -0.068 (one layer), -0.136 (two layers), -0.204 (three layers), -0.272 (four layers) and -0.34 (five layers). Figure 4a shows the contrast spectra of graphene with various layers. The intensity of the contrast from varied graphene layers can be unambiguously determined. Fig. 4b shows Raman spectra of graphene on quartz with varied number of layers. The prominent G band at 1584 cm^{-1} and 2D band at 2689 cm^{-1} are clear resolved. The relatively weak D band at 1344 cm^{-1} indicates less defects and high crystallinity of as produced graphene.

The misoriented layers in the graphene sample result in different Raman features from AB stacking graphene. We found that 5 layers graphene even has narrow and symmetric 2D band with width of 28.8 cm^{-1} (inset of Fig. 4b), comparable to AB stacking monolayer graphene. This suggests that the misoriented multilayer graphene has similar electronic structure with single layer graphene.

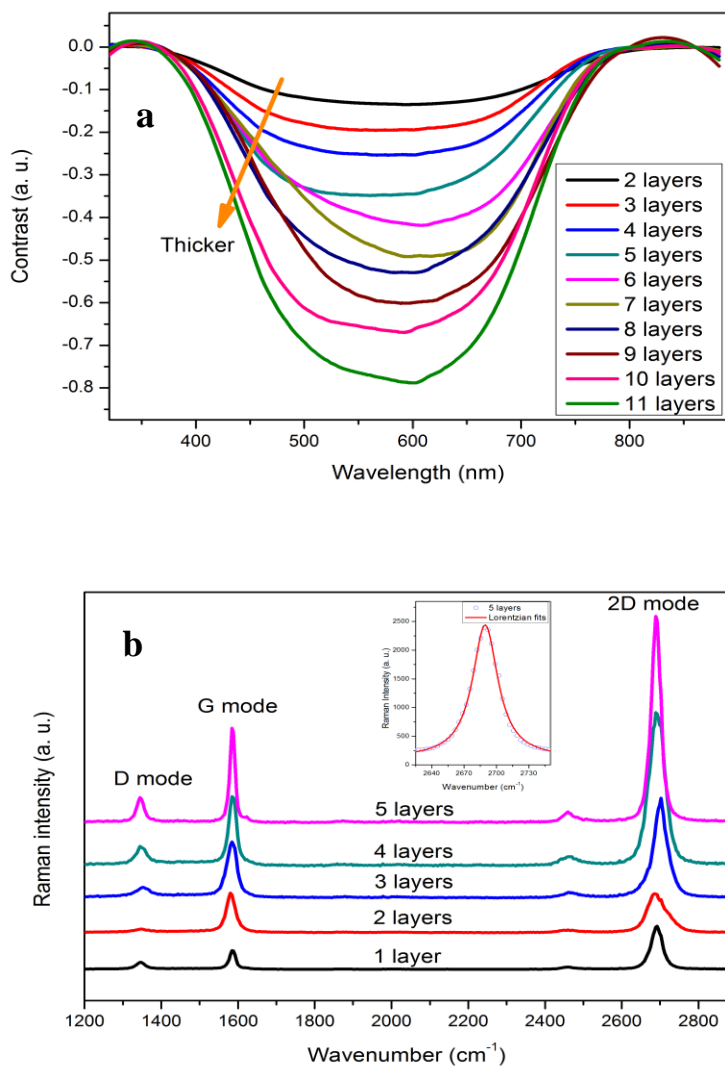


Figure 4. (a) Contrast spectra of graphene sheets with different thickness. (b) Raman spectra as a function of the number of graphene layers. Inset shows Lorentzian fitting of 2D band of 5 layers graphene.

3.2 Fabrication of graphene derivatives and graphene-polymer nanocomposites

In order to achieve the optimized mode locking performance of a laser, the parameters of a saturable absorber, these are the saturable modulation strength and saturation recovery time, must match to the particular properties of the laser gain medium and the laser cavity. Frequently there is a need to fine-tune the saturable absorption parameters of the absorbers. For atomic layer graphene this fine tune might be achieved through chemical functionalization technique. As the few layer graphene have only nanometer thickness, it is also not convenient to use in many cases. Therefore, if the graphene based saturable absorber could be made as a freestanding membrane, it will be user-friendly. For these purposes in the project we have also studied the saturable absorption of the graphene derivatives and graphene-polymer nanocomposites. Our strategy is to incorporate functionalized graphene nanoflakes into polymer nanofiber by electrospinning. The as-produced graphene-polymer mat not only provides a free-standing membrane with appreciable mechanical strength for transferring onto any optical components for variant applications, but also affords protections from photo-oxidation and optical bleaching.

Four types of graphene derivatives were studied. These are the graphene-oxide (GO), GO non-covalently bonded with poly(p-phenylenevinylene) (GO-PPV), graphene modified by 1-pyrenebutanoic acid, succinimidyl ester (G-PBASE) and graphene functionalized with 4-(2-(pyridin-4-yl)vinyl) phenyl group (G-dye). PPV has been widely investigated because of its nonlinear optical response and electroluminescent activity. The functionalization of GO with PPV is expected to impart nonlinear optical properties on the composite. PBASE has been used extensively for the non-covalent functionalization and solubilisation of carbon nanotubes due to its hydrophilic character. The π - π stacking interaction between the pyrene moiety and graphene allows graphene to maintain the conjugated network, at the same time, the attachment of PBASE provides the succinimidyl ester groups which impart solubility on the system. The dye which is covalently coupled to graphene has a Donor- π -Acceptor structure. It is a highly π -conjugated chromophore, which contains a pyridium moiety (acceptor). The pyridium salt helps to improve the solubility of the systems by introducing electron-withdrawing group which stabilizes the electron-rich phenylethyl core, and prevents aggregation.

The various graphene derivatives are synthesized as following: **GO**. A conical flask equipped with a magnetic stir bar was charged with 69 ml H_2SO_4 , and cooled to 0-5 °C by immersion in an ice bath. 1.5 g graphite was then added slowly with vigorous stirring while still maintaining the reaction at 0-5 °C. After the graphite was well dispersed into black slurry, 1.5 g NaNO_3 was added slowly over 15 min at 0-5 °C. The mixture was allowed to warm to room temperature and stirred for 1h. 120 ml water was added, and the solution was stirred for 30 min while the temperature was raised to 90 °C. The mixture was poured into 300 ml water, followed by the slow addition of 10 ml of H_2O_2 . The colour of the solution changed from dark brown to yellow. The solution was then filtered. The material was re-dispersed in water, and washed by water until the PH of the filtrate was neutral according to PH indicator paper. The resultant GO material was then dried in a vacuum desiccator overnight at room temperature and stored in ambient environment. **GO-PPV**. GO (1mg) was dispersed in 10 ml N, N-dimethylformamide (DMF) by sonication. Then, 1 mg PPV were added to the dispersion and heated to 80 °C for 24 hours. Ethanol (50ml) was added to the product before centrifuging to obtain GO-PPV. The GO-PPV obtained was washed with ethanol before drying under vacuum. **G-PBASE**. GO (1mg) was dispersed in 10 ml DMF by sonication. Following, 1 mg PBASE and 100 μL hydrazine monohydrate were added to the dispersion and heated to 80 °C for 24 hours to facilitate reduction of GO. Ethanol (50 ml) was added to the product before centrifuging to obtain graphene-PBASE. The graphene-PBASE obtained was washed with ethanol before drying under vacuum. **G-dye**. Synthesis of G-dye involved the complete exfoliation of graphite into individual GO sheets, followed by reduction to produce individual graphene sheets (RG). The RG was functionalized with the phenyl bromide group using diazonium coupling reaction, and then reacted with 4-vinylpyridine using Heck reaction.

To make the membrane, as synthesized graphene derivatives (0.47 mg) was dispersed in DMF (1 ml) by ultrasonication. Then the solutions were mixed with 3 ml 23.5 wt% PVAc in DMF and then stirred for 24 hours at 60 °C in sealed bottles to form the wet paste for electrospinning. The electrospinning was carried out in MECC NANON ELECTROSPINNING set up with the highest bias voltage of 30 kV. The optimized electrospinning parameters are: applied voltage of 30 kV, feeding rate of 0.5 ml h^{-1} and

the needle tip to collector distance of 100 mm. During electrospinning, the needle scanned above the collector of aluminum foils for 5 min to form a membrane with size of $150\text{ mm} \times 20\text{ mm}$ and thickness of around $10\text{ }\mu\text{m}$. A schematic of the fabrication process is shown in Fig. 5.

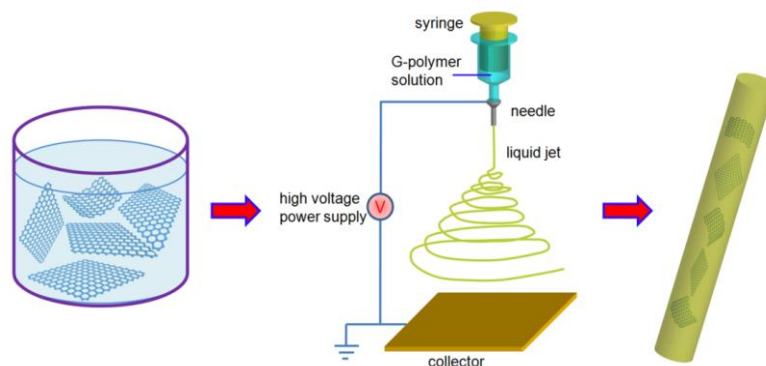


Figure 5: Schematic illustration of the fabrication of graphene-polymer nanofiber composite by electrospinning.

The morphologies of G-polymer nanocomposite were investigated by optical microscopy and scanning electron microscopy (SEM, JSM-6700F, JEOL, Japan). The microstructure of the graphene-polymer nanocomposite was characterized by transmission electron microscopy (TEM, JEOL 3010, 200 kV, Japan). The G-polymer nanofibers were directly electrospun on carbon coated copper grids for TEM investigation. Optical absorption spectra from UV to near infrared region were obtained using a Shimadzu 3200 spectrometer.

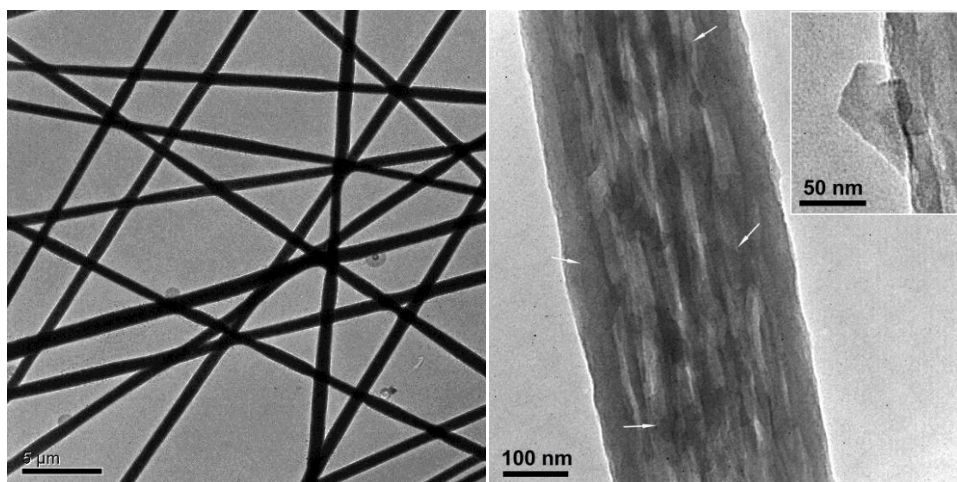


Figure 6: a) TEM image of G-PBASE-PVAc nanofibers. b) High magnification TEM image of G-PBASE-PVAc nanofiber. The arrows indicate the graphene flakes inside nanofiber. The inset shows enlarged image of G-PBASE embedded in sidewall of PVAc nanofiber.

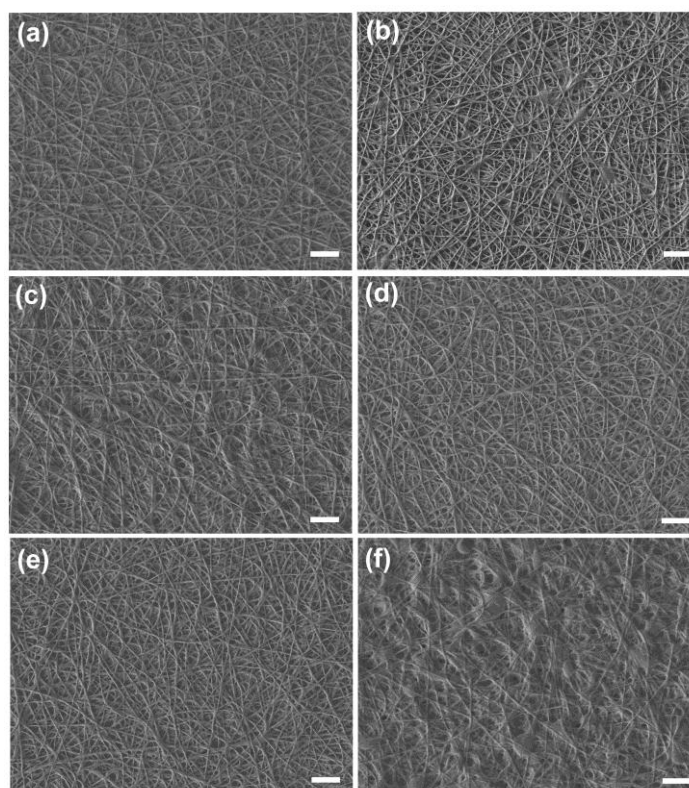


Figure 7: SEM images of electrospinning graphene-polymer nanocomposite membrane. a) Pristine PVAc, b) GO/PVAc, c) GO-PPV/PVAc, d) G-PBASE-PVAc, e) G-dye-PVAc. f) SWNT/PVAc. Scale bars in all images: 10 μm .

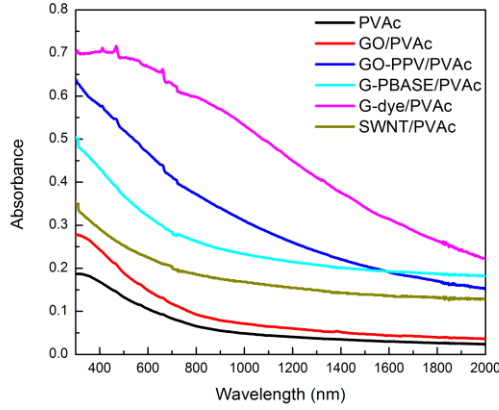


Figure 8: UV-vis-NIR absorption spectra of graphene-based PVAc nanocomposites.

3.3 Graphene saturable absorption measurement

The saturable absorption measurement setup used is shown in Fig. 9. A standard soliton mode locked fiber laser with output pulse width of 1 ps and repetition rate of 100 MHz was used as the light source. The seed pulses were amplified with an erbium doped fiber amplifier (EDFA). To reduce the errors caused by the fluctuation of the input power, the output powers (with or without passing through graphene) were measured simultaneously through two sets of power meter with equal optoelectronic response and parameter settings, e.g. sweeping time, as shown in Fig. 9.

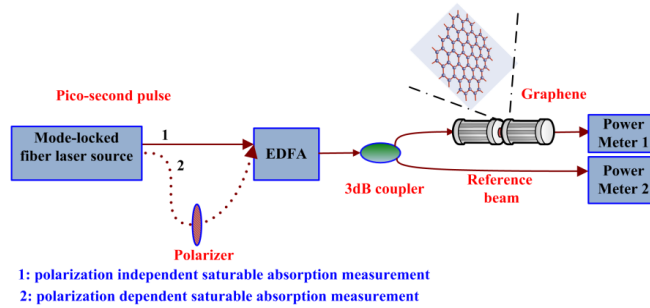
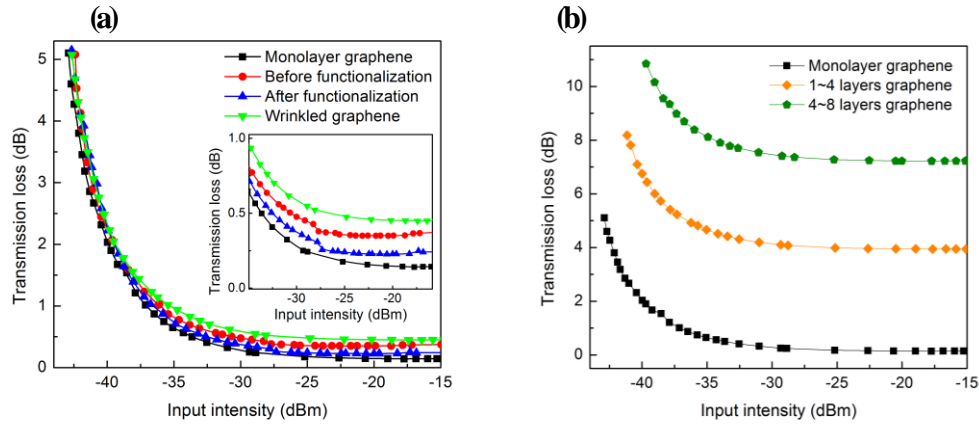


Figure 9. Experimental setup for measuring nonlinear power dependent absorption of graphene samples.

We measured the saturable absorption of the following types of graphene samples:

monolayer graphene, monolayer graphene covalently bonded to functional groups on its basal plane by diazonium functionalization, monolayer graphene with wrinkles, as well as 1~4 layers and 4~8 layers graphene grown on Ni. The remarkable result is that pristine monolayer graphene has a normalized modulation depth of 95.3%, which is much larger than those of the few layer graphene. However, under existence of surface defects (wrinkles) or for thicker graphene the normalized modulation depth becomes smaller. After functionalization, the modulation depth is enhanced a little bit from 89.5 % to 93.6 %. The saturation intensity shows the opposite trend versus surface defects and graphene thickness. The pristine monolayer graphene has the smallest saturation intensity of 0.53 MW cm^{-2} , while two small wrinkles on the surface (shown in Figure 1b) leads to 4% increase of the saturation intensity. The 1-4 layers graphene film has a saturation intensity of 0.77 MW cm^{-2} . Scaling with thickness, the 4-8 layers graphene needs much more incident light power to reach saturation with a saturation intensity of 1.09 MW cm^{-2} . It is believed that the defect induced nonsaturable loss and scattering play a dominant role on affecting the saturation intensity.



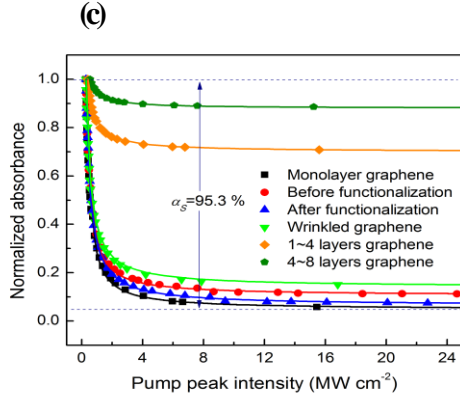


Figure 10: Power-dependent nonlinear absorption properties. (a) Monolayer graphene samples with different surface states. Inset shows enlarged plots. (b) Comparison of monolayer graphene with multilayer graphene. (c) Normalized power-dependent nonlinear saturable absorption properties.

The polarization dependence of the graphene saturable absorption was also experimentally measured. A similar measurement setup as shown for the polarization independent saturable absorption of graphene was used. However, the incident laser pulses were first passed through a polarizer so that a linearly polarized light with a fixed polarization state was used as the input light. The saturable absorption of graphene samples under illumination of orthogonally polarized light was then measured. To reduce any artificial discrepancy caused by the fluctuation of the input power, output powers (with or without passing through the graphene sample) were detected simultaneously using two power meters of the same type. Fig. 11 shows the measured polarization dependence of the graphene saturable absorption. The same normalized modulation depth of ~66 % for both polarizations was observed. The measured saturable fluences for the two polarizations are ~0.71 MW cm⁻² and ~0.70 MW cm⁻², respectively, which is well within the measurement error range. The experimental result demonstrates that graphene could be reasonably regarded as a polarization insensitive saturable absorber.

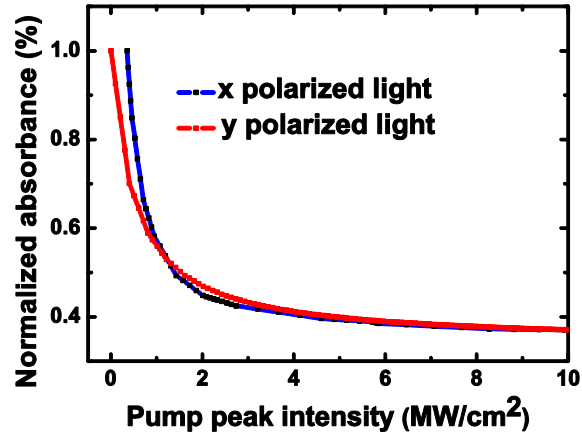


Figure 11: Polarization dependent saturable absorption curve of graphene-based mode locker.

3.4 Fabrication of graphene based laser mode lockers

Different forms of the graphene based laser mode locker were made. For the purpose of using graphene to mode lock fiber lasers, we have made either the transmission type or the reflection type of mode lockers. To make a transmission form of fiber laser mode locker, we simply transfer the graphene film onto the end of a fibre pigtail: the cross-section of the fibre pigtail is kept parallel to the surface of the floating graphene film, then it was gently dip onto the graphene film and slowly dried in cabinet. Fig. 12 shows a fibre pigtail with graphene film (gray color area) coated on the fiber end. Optical image shown in Fig 12b shows that the whole pinhole (including outer cladding with diameter of $\sim 100\ \mu\text{m}$ and inner core with diameter of $5\text{-}10\ \mu\text{m}$) was covered by a large area graphene film.



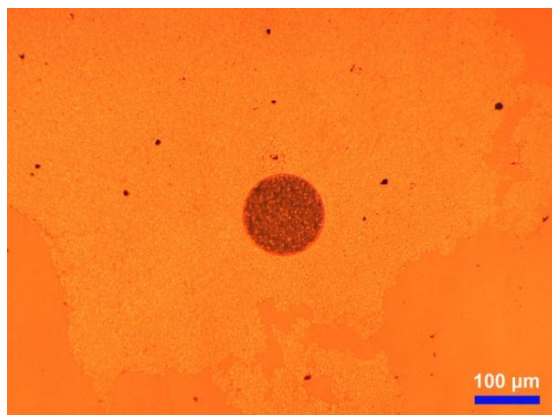


Figure 12: a) Photograph of optical fiber with graphene film (gray color area) coating on the pigtail cross-section. (b) Optical image of large area graphene film covering on the fibre pinhole (red colour circle area at the center).

Raman spectroscopy was used to evaluate the quality and uniformity of graphene in fiber core area, as shown in Figure 13. The location of the $\sim 8 \mu\text{m}$ fiber core is determined by Raman signal in the $200 - 600 \text{ cm}^{-1}$ range, which originates from crystalline SiO_2 core. Figure 13 shows that monolayer graphene film covers quite homogeneously on the fiber core-area.

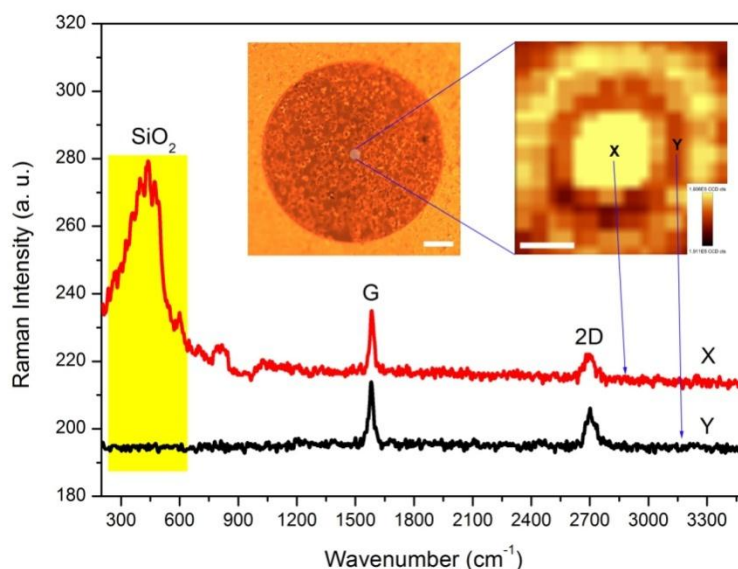


Figure 13: Raman spectra from fibre core area. Inset: optical image of fibre pinhole (left) and Raman image (right) of fibre core plotted by the intensity of the band between $200 - 600 \text{ cm}^{-1}$ (yellow color region). The Raman spectra X and Y represents the Raman signals from the location of X and Y in the Raman image.

To make the graphene based saturable absorber mirror (SAMs), we just simply transferred a large size graphene grown with the CVD method onto a dielectrically coated mirror. Fig. 14 shows a photo of a graphene saturable absorber mirror (GSAM). The graphene film on the mirror is clearly visible.

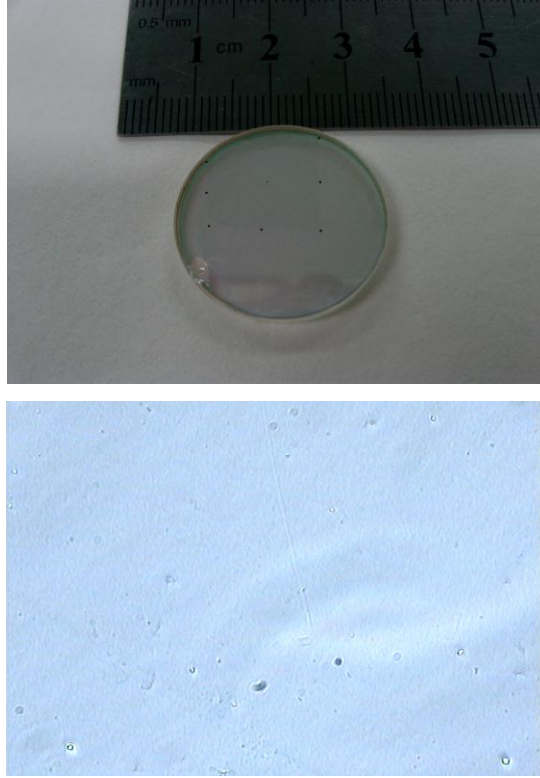


Figure 14: a) photograph of a graphene saturable absorber mirror. The atomic layer graphene is within the area ($\sim 1 \text{ cm}^2$) marked by the black dots. B) Microscopic image of the graphene. It shows that the graphene is quite uniform.

Graphene polymer nanocomposite thin films with different thickness were fabricated. Fig. 15 shows a photo of the film. To use the thin film saturable absorber for mode locking, it is cut into a desired size and inserted between two fibers connected with the ferule connector.

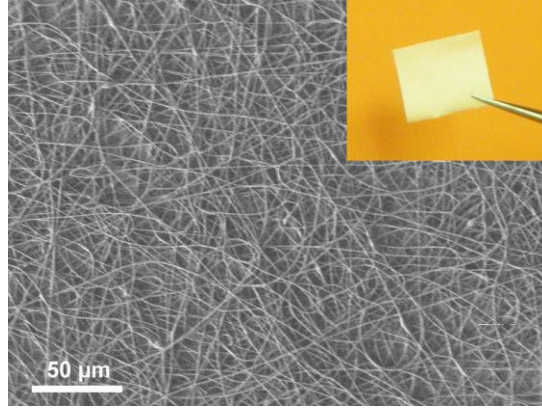


Figure 15: SEM image of the graphene-polymer nanofiber networks. Inset: photograph of the freestanding graphene-polymer composite membrane.

4. Mode Locking of lasers with atomic layer graphene

4.1 Graphene mode locked soliton fibre lasers

We first experimentally investigated passive mode locking of the erbium-doped fiber lasers with graphene as saturable absorber, and successfully achieved self-started mode locking of the lasers. A ring fiber laser configuration as schematically shown in figure 16 was used. A piece of 5.0 m, 2880 ppm Erbium-doped fiber (EDF) with group velocity dispersion (GVD) of -32 (ps/nm)/km was used as the gain medium, the other fibers used are either the standard single mode fiber (SMF) with GVD of 18 (ps/nm)/km or the dispersion shifted fiber (DCF) with GVD of -2 (ps/nm)/km. An optical circulator was used in the cavity to incorporate the graphene saturable absorber mirror (GSAM) into the cavity, and a lens fiber, fixed on a XYZ translation stage, was used to collimate the light from the fiber and collect the reflected light from the GSAM. The insertion loss of the GSAM is about 3 dB. A 30% fiber coupler was used to output the signal, and the laser was pumped by a high power Fiber Raman Laser source (KPS-BT2-RFL-1480-60-FA) of wavelength 1480 nm. An intra-cavity polarization controller (PC) was used to fine-tune the linear cavity birefringence. The GSAM was made of multi-layer graphene.

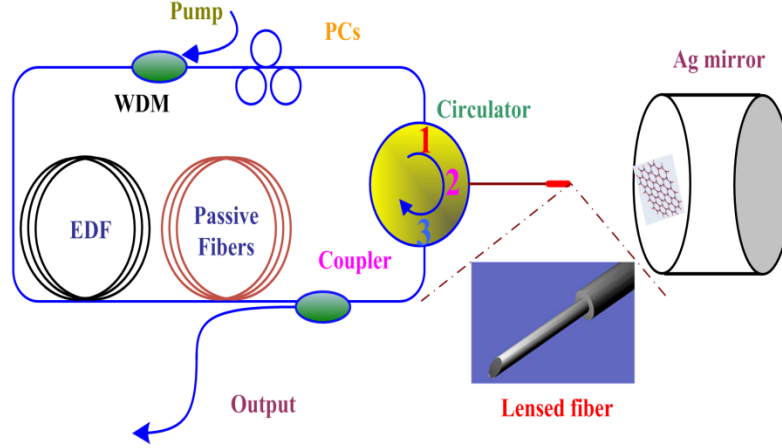


Figure 16: Schematic of the GSAM mode locked erbium-doped fiber laser

The fiber laser has a so-called dispersion-managed cavity design. The normal dispersion gain fiber was used to avoid the pulse collapse effect within the gain medium. Through changing the SMF length, we have changed the net cavity dispersion of the fiber laser so the laser could either operate in the net positive or net negative cavity dispersion regime. We first operated the fiber laser at a net negative cavity dispersion of about -0.3419 ps^2 (with a piece of $\sim 23.4 \text{ m}$ SMF). Self-started mode locking was obtained as an incident pump power of $\sim 130 \text{ mW}$ (intra-cavity power of $\sim 43 \text{ mW}$). Figure 17 shows a typical mode locked state of the laser. Fig. 17a is the oscilloscope trace of the mode locked pulse train (in nanosecond and millisecond time scale, respectively). The pulses have a fundamental repetition time of $\sim 200 \text{ ns}$, determined by the cavity length. Fig. 17b shows the measured RF spectrum of the pulses, which has the fundamental peak located at $\sim 5.0 \text{ MHz}$ with a signal-to-noise ratio of 50 dB (10^5 contrast). Fig. 17c shows the optical spectra of the mode locked pulses. On their spectrum Kelly sidebands are clearly seen, indicating that the pulses have already been shaped into optical solitons. The graphene mode locked fiber laser has shown exactly the same feature, indicating that the graphene mode locker played the same role as those of the other types of mode lockers such as the SESAM, CNTs etc. Fig. 17d gives the autocorrelation trace of the mode locked pulses. It shows that the pulse duration is $\sim 1.3 \text{ ps}$ if a Sech^2 -pulse profile is assumed. The time-bandwidth product of the pulses is ~ 0.325 . The pulses are almost transform-limited. Fig. 17e shows the input-output relation of the laser emission. An

output power up to 7.8 mW was obtained in the laser with a slope efficiency of $\sim 10\%$.

Under strong pumping multiple soliton pulses were always obtained. However, by carefully reducing the pump power the number of soliton could be reduced one by one. It was measured that the maximum single pulse energy of the laser is ~ 1.5 nJ. Depending on the laser cavity parameter selection, a noise-like pulse mode locking state was also observed, where the mode locked pulse spectra has broadband smooth spectra similar to those observed in the NPR mode locked lasers.

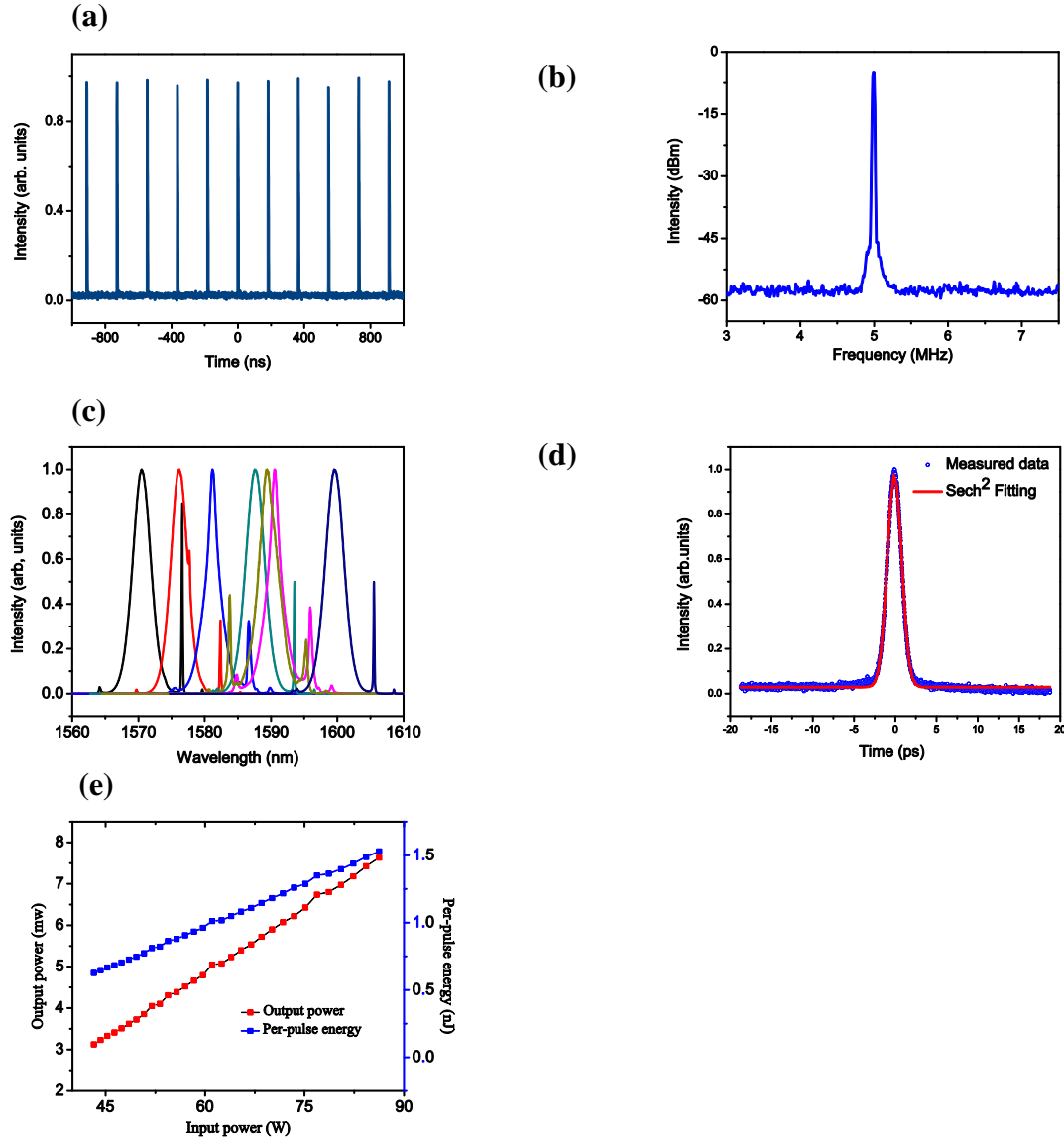


Figure 17: A typical state of the GSAM mode locked net-anomalous-dispersion cavity fiber laser. (a) Output pulse train. (b) Radio frequency spectrum. (c) Optical spectra. It is tunable from 1570 nm to 1600

nm. (d) Autocorrelation trace and the Sech^2 fitting. (e) Output power and per-pulse energy as a function of pump power: a maximum of 1.5 nJ was obtained.

Fig. 17c also shows the wavelength-tuning feature of the graphene mode locked fiber laser. As graphene has super broadband saturable absorption, if a wavelength tunable bandpass filter is inserted in the laser cavity, mode locking at different central wavelengths could be achieved. Eventually wavelength tunable mode locking is obtained. In our experiment we used the birefringence filter property of the fiber cavity to achieve the wavelength tuning of the solitons. A continuous soliton wavelength tuning of $\sim 30\text{nm}$ was achieved in the erbium-doped fiber laser.

We have also operated the fiber laser in the net positive cavity dispersion regime (with a net cavity dispersion of -0.583ps/nm). It was found that mode locking could still be achieved with a GSAM as a mode locker. Fig. 18 shows a typical mode locked state of the laser. In the normal dispersion regime mode locking of the fiber lasers has a notably higher pump threshold. Fig. 18a shows the optical spectrum of the mode locked pulses. It has steep spectral edges, which is a typical feature of the dissipative solitons formed in the normal dispersion fiber lasers. The peak wavelength in Fig. 18a is $\sim 1589.3\text{ nm}$ and the 3 dB spectral bandwidth is $\sim 12\text{ nm}$. The dissipative solitons have a pulse width of $\sim 32.9\text{ ps}$, indicating that the observed dissipative soliton pulse has a time-bandwidth product of ~ 49.35 and is strongly chirped. Fig. 18c shows the oscilloscope trace of the mode locked pulse train. It has a pulse separation of $\sim 638\text{ ns}$, equals to $\sim 1.57\text{ MHz}$ as shown in Fig. 18d. Fig. 18e shows the input-output power relation of the laser under the single pulse emission. The output power increased linearly with the injected pump power. A maximum output power of $\sim 23.9\text{ mW}$ was obtained, which shows a single pulse energy of $\sim 15.2\text{ nJ}$. At the maximum output power, the pulse width is $\sim 33\text{ ps}$, which gives the maximum peak power of $\sim 0.46\text{ kW}$.

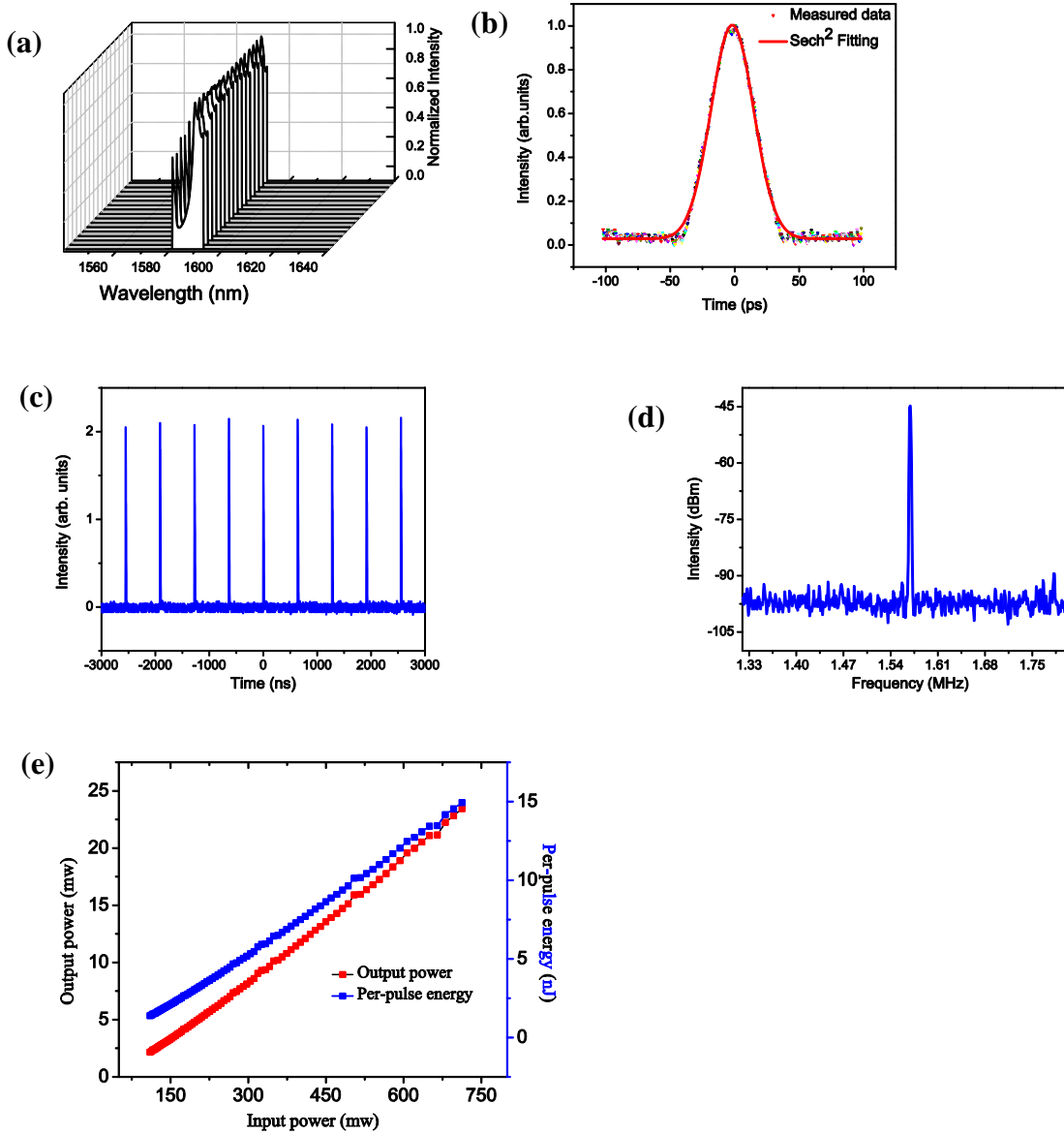


Figure 18: A typical mode-locking state of the normal dispersion cavity fiber laser mode locked by a GSAM. (a) A long-term spectral recording of the dissipative soliton spectrum measured at a 4-hour interval over 2 days. (b) Autocorrelation trace and the Sech² fitting curve. (c) Output pulse train. (d) Radio frequency spectrum. (e) Output power and single pulse energy as a function of the injected pump power.

Multiple dissipative solitons could still be obtained in a normal dispersion fiber laser, comparing with the soliton operation of an anomalous dispersion fiber laser, significantly larger mode locked single pulse energy could be obtained in fiber lasers with net positive cavity dispersion.

4.2 Vector soliton operation of the graphene mode locked fiber lasers

A property of the graphene mode locker is that its saturable absorption is polarization insensitive. This feature in combination with the weak birefringence of the single mode fibers could be exploited to generate vector solitons in the mode locked fiber lasers. Compared with the conventional scalar solitons obtained in fiber lasers, a vector soliton has two coupled orthogonal polarization components. As in order to obtain the vector soliton operation in a mode locked fiber laser no any polarization sensitive component could be in the cavity, which excludes the nonlinear polarization rotation mode locking possibility in a fiber laser, the vector soliton operation of graphene mode locked fiber lasers further confirms the graphene mode locking effect.

We used a fibre laser configuration as schematically shown in Fig. 19 to investigate the vector soliton operation of the graphene mode locked fibre lasers. The laser cavity is a ring that consists of 0.7 m erbium-doped fibre (EDF Er80-8/125 from Liekki) with group velocity dispersion (GVD) of $-22 \text{ fs}^2/\text{mm}$ and 22 m standard SMF. A 10% fibre output coupler was used to output the signal, a polarization independent isolator was used to force the unidirectional operation of the ring cavity, and an intra-cavity polarization controller (PC) was used to fine tune the linear cavity birefringence. All passive components are made of the SMF or pigtailed with SMFs. Their polarization losses were checked to make sure to be sufficiently small. The laser was pumped by a high power Raman fibre laser (KPS-BT2-RFL-1480-60-FA) of wavelength 1480 nm. The graphene used was fabricated with the chemical vapour deposition and the graphene sheets were deposited on a standard FC/PC fibre connector. It is estimated that the graphene used has 3~5 atomic layers with a saturable absorption modulation depth of ~23%. To experimentally identify the vector soliton operation of the fibre laser, an in-line polarization beam splitter (PBS) was used to separate the two orthogonal polarization components of a vector soliton.

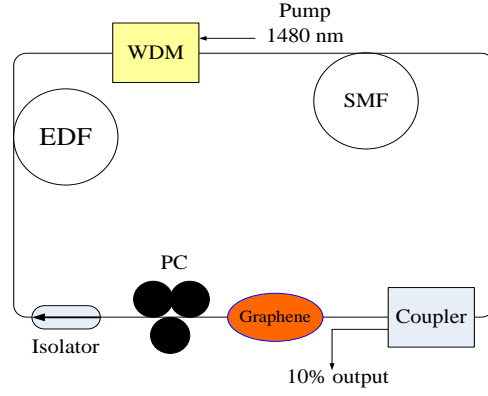
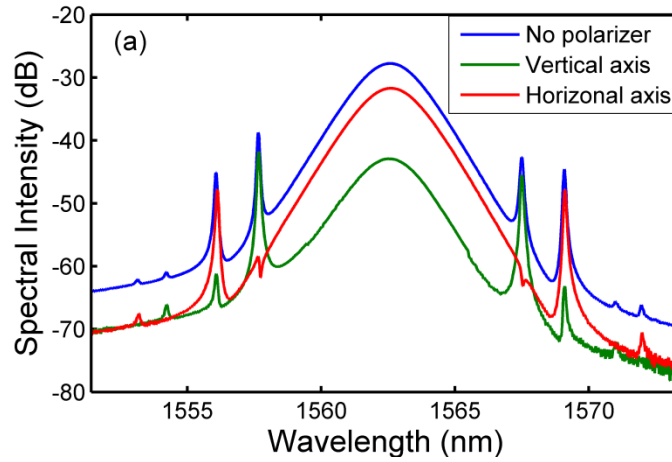


Figure 19: A schematic of the experimental setup. PC: Polarization controller, EDF: Erbium doped fiber, SMF: Single-mode fiber, WDM: Wavelength-division multiplexer.

As the laser cavity has only weak net birefringence, it was found that whenever the laser was mode locked, the vector solitons would be obtained. Through carefully changing the net linear cavity birefringence or adjusting the soliton pulse intensity, various types of vector solitons were experimentally obtained in the laser.



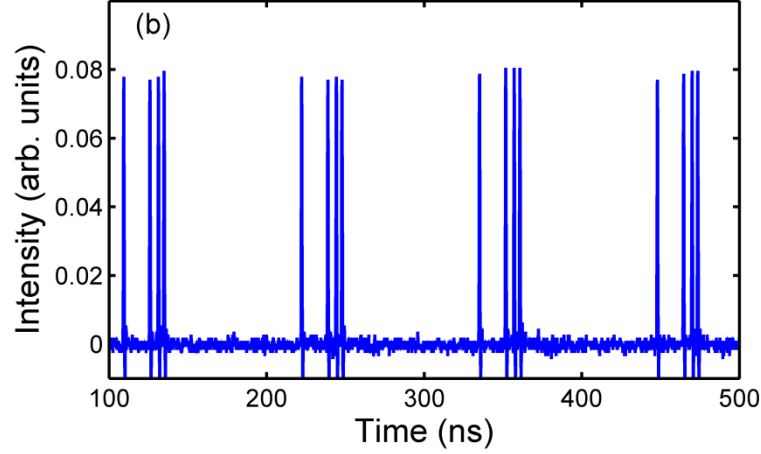


Figure 20: Vector soliton emission of the fiber laser. (a) Soliton spectra. Blue line: the total laser emission without passing through a polarizer; Red line, Components along the vertical axis; Green line, component along the horizontal axis. (b) Oscilloscope trace.

Fig. 20 shows for example the phase locked vector soliton operation of the fiber laser. Figure 20(a) is the measured optical spectrum. Kelly sidebands are obvious on the soliton spectrum, confirming that the pulses are optical solitons. The central wavelength of the solitons is at 1562.40 nm. Fig. 20(b) is the measured oscilloscope trace of the soliton pulses. In the state all the pulses in cavity have exactly the same pulse height, indicating that the solitons possess the soliton energy quantization property. Different from the soliton spectra obtained on the scalar solitons formed in fiber lasers, apart from the Kelly sidebands there are also another set of spectral sidebands on the soliton spectrum. At first sight one may confuse all the sharp spectral peaks on the soliton spectrum as the Kelly sidebands. However, as one carefully adjusts the intra cavity PC, it will be observed that one set of the spectral sidebands shifts their positions remarkably on the soliton spectrum, while the other set of spectral sidebands have almost no position change. The latter set of spectral sidebands is the Kelly sidebands, while the appearance of the other set of spectral sidebands is a result of the vector soliton operation. The difference of the spectral sidebands is better identified through measuring the polarization resolved spectra of the vector solitons. As shown in Fig. 20(a), on the polarization resolved spectra while the Kelly sidebands always exhibit as spectral peaks, the other set of spectral sidebands displays either as a spectral peak or a spectral dip, indicating the existence of coherent energy exchange between the two soliton components. Formation

of such spectral sidebands is due to the coherent coupling between the two polarization components of the vector solitons in the laser. Fig. 21 shows the polarization resolved oscilloscope traces of a polarization locked vector soliton operation state.

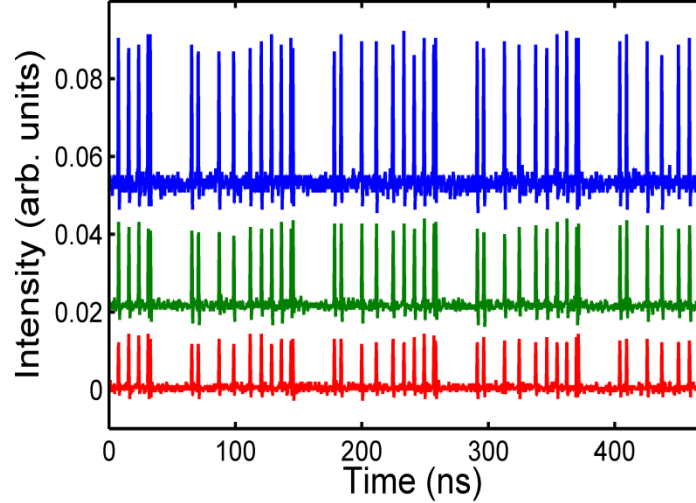


Figure 21: Oscilloscope traces of pulse train in a phase locked vector soliton operation state. Upper trace: the vector soliton evolution. Middle trace: the vertical polarization component. Lower trace: the horizontal polarization component.

Fig. 22 shows the polarization resolved measurements of the polarization rotation vector solitons. Unlike the polarization locked vector solitons, where the polarization of the solitons emitted by the laser is fixed, the polarization of the solitons rotate along the cavity and varies from pulse to pulse. The polarization rotation feature of the solitons is obviously reflected in Fig. 22. Without passing through an external cavity polarizer, the soliton pulse train has a uniform pulse height, while after passed through the PBS the pulse height becomes periodically modulated. In particular, the periodic pulse height modulation for each of the orthogonal polarization directions is different. The pulse height returns back to its original value after several cavity round trips.

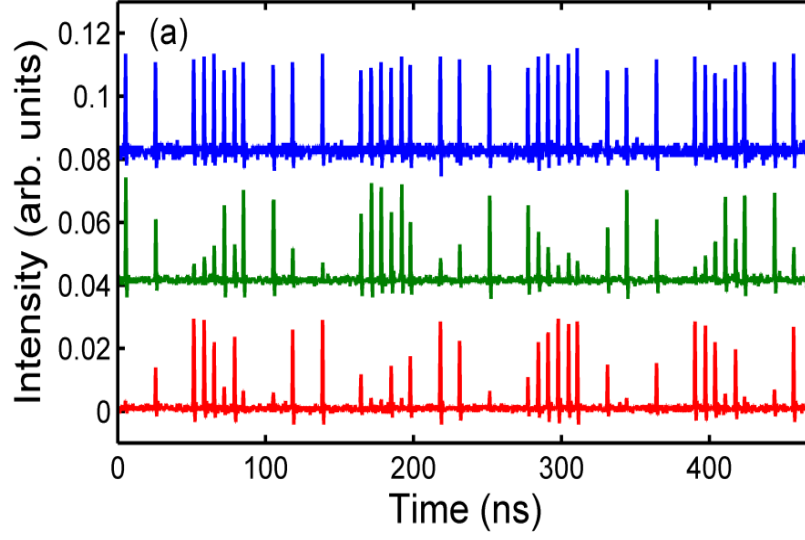


Figure 22: Oscilloscope traces of a polarization rotation vector soliton operation state of the laser. Upper trace: the vector soliton evolution. Middle trace: the vertical polarization component. Lower trace: the horizontal polarization component.

Like the appearance of Kelly sidebands is a characteristic of the soliton formation in a laser, we found that the appearance of the above extra spectral sidebands is a characteristic of the vector soliton formation in our fiber laser. Experimentally, we further noticed that once the vector soliton polarization rotated, two new sets of spectral sidebands further appeared on the soliton spectrum, as shown in Figure 23.

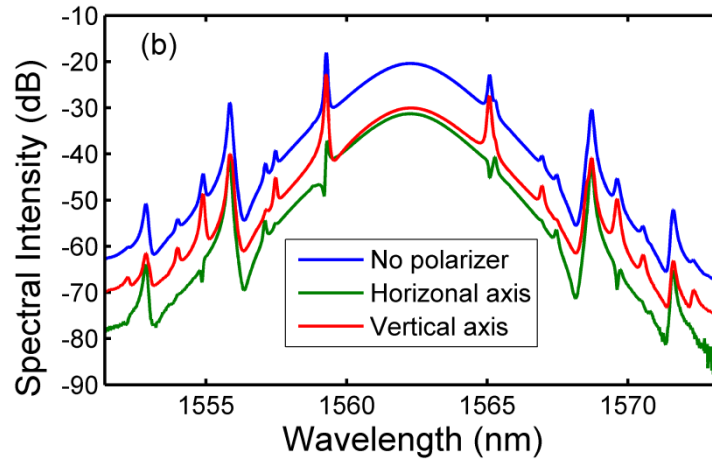


Figure 23: A polarization rotation vector soliton state of the laser. (a) The total and the polarization resolved soliton pulse trains with multiple solitons in cavity. (b) Optical spectra of the solitons. Blue

line: the total laser emission without passing through a polarizer; Red line: component along the vertical axis; Green line: component along the horizontal axis.

Comparing Fig. 23 with Fig. 20(a) it is to see that apart from the Kelly sidebands, there are another three sets of spectral sidebands visible on the soliton spectrum now. Based on the polarization resolved spectra, one set of the sidebands is due to the coherent energy exchange between the two orthogonal polarization components, as described above. Each of the other two sets of the weak new sidebands appears only on spectrum of one of the two orthogonal polarization components, respectively. Moreover, no matter how the two orthogonal polarization components are split, the weak new sidebands are always spectral peaks. No spectral dip could be obtained. The feature of the weak new sidebands is similar to that of the Kelly sidebands. The two new sets of weak spectral sidebands were formed due to the polarization rotation of the vector solitons. The periodic polarization rotation of the vector solitons introduces an extra periodic soliton parameter variation, therefore, leads to the formation of another set of Kelly sidebands. As the soliton polarization rotation has a different period than that of the soliton circulation in the cavity, the new Kelly sidebands have different positions to those of the conventional Kelly sidebands. The formation of Kelly sidebands is a linear effect, which is caused by the constructive interference between the dispersive waves emitted by the solitons circulating in the cavity. For a vector soliton it has two orthogonal polarization components, in a state of polarization rotation each soliton polarization component would have different phase. It could be due to the subtle difference between the two polarization components that each soliton component formed its own Kelly sidebands under the periodic soliton polarization rotation.

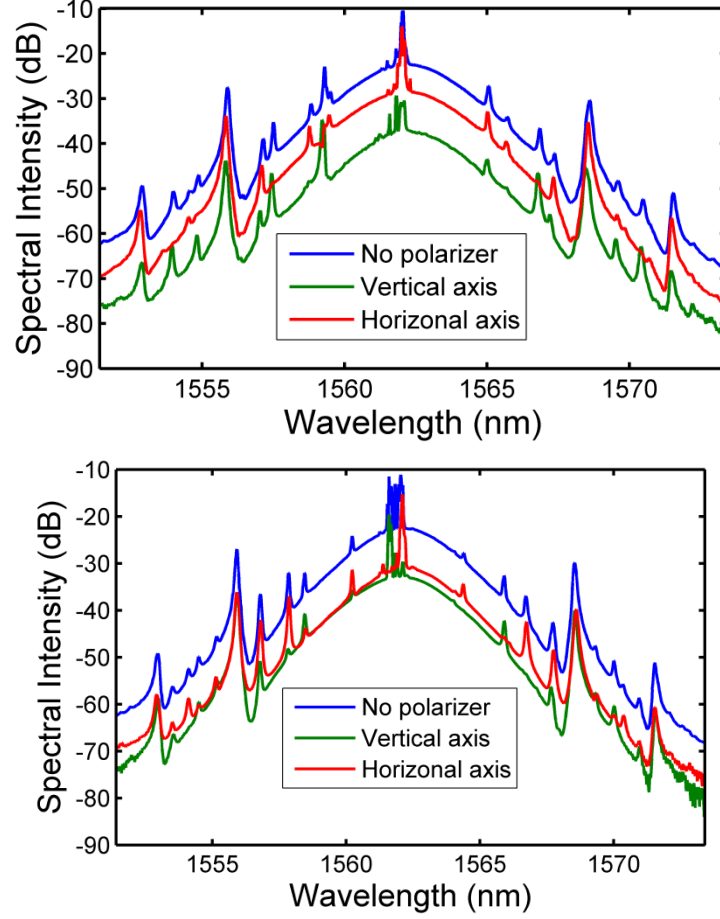


Figure 24: Vector soliton spectra of the fiber laser under quasi-periodic vector soliton intensity variation. Blue line: the total laser emission without passing through a polarizer; Red line: component along the vertical axis; Green line: component along the horizontal axis.

Because the solitons formed in a laser are dissipative in nature, their soliton pulse energy increases with the pump power. Experimentally it was found that under certain laser conditions, when the energy of the vector solitons increased to a certain level, an extra set of spectral sidebands further appeared on the vector soliton spectrum, as shown in Fig. 24. In addition, the pulse height of the vector solitons on the oscilloscope trace also gradually became non-uniform as shown in Fig. 25. Based on the polarization resolved soliton pulse traces, it is identified that the polarization rotation of the vector soliton also became quasi-periodic.

Two different situations were revealed through the polarization resolved measurements. Fig. 24a shows a case where the vector soliton has a large polarization ellipse. In this case the new extra spectral sidebands only appeared on the strong polarization component of the vector soliton. On spectrum of the weak polarization component there is no sign of the new extra spectral sidebands. Fig. 24b shows another case where the strength of the two orthogonal polarization components of the vector soliton was comparable. In this case the new extra spectral sidebands appeared at the same position on both polarization components. This experimental result suggests that the appearance of the new extra spectral sidebands is a threshold effect. Its appearance requires that the pulse intensity of the soliton is sufficiently strong. In addition, comparing the results shown in Fig. 24a, b, which were taken under two different intracavity PC settings but the same pump power, the positions of the new extra spectral sidebands also depend on the laser cavity detuning.

Based on our past research experience on the various spectral sideband formation on the optical spectra of the scalar solitons in fiber lasers, the new set of spectral sidebands was attributed to the modulation instability effect of the vector solitons. Under effect of the soliton modulation instability the energy of the soliton and dispersive waves are coherently coupled. Under strong coherent energy coupling the energy of the soliton then becomes varying as it propagates in the cavity. Therefore, its energy becomes quasi periodically varying with the cavity roundtrips.

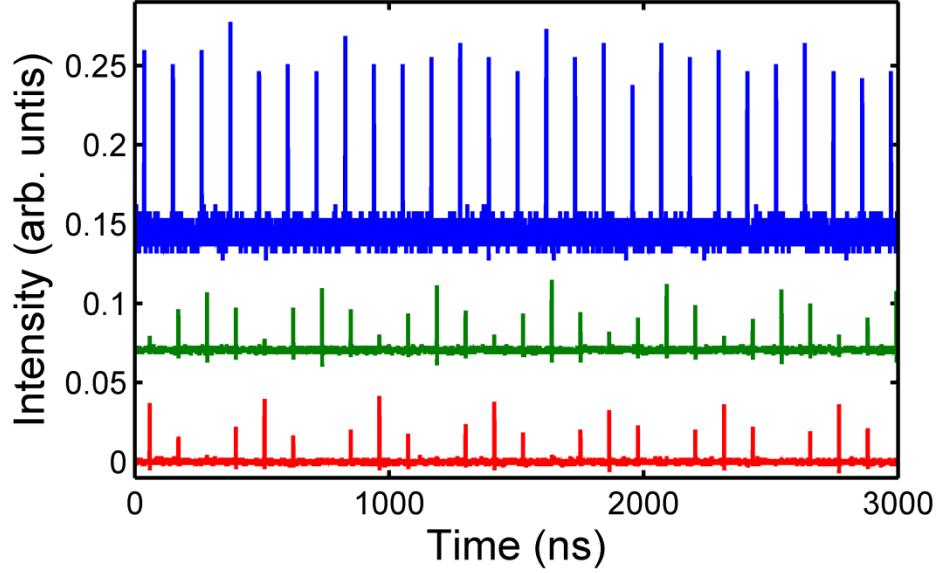


Figure 25: Oscilloscope traces of the vector solitons under quasi-periodic vector soliton intensity variations. Upper trace: the vector soliton evolution. Middle trace: the vertical polarization component. Lower trace: the horizontal polarization component.

The soliton MI is a threshold effect. Like the case of scalar solitons, once the intensity of the vector solitons became beyond the MI threshold, a new set of spectral sidebands appeared at the positions where the phase matching condition between the soliton and dispersive waves is fulfilled. However, different from the scalar solitons, a vector soliton has two coupled orthogonal polarization components. Further depending on the strength of them, either both of the two polarization components or one of them could become unstable. Nevertheless, either case would lead to the quasi-periodic evolution of the vector soliton. Because the coherent wave mixing is between the soliton and dispersive waves, no spectral dip-peak but only the spectral peaks were observed on the polarization resolved spectra.

From a quasi-periodic vector soliton evolution state, if the pump power was further increased, instead of that the laser emission evolved to the chaotic state, a new soliton was then generated, eventually the vector soliton evolution became periodic or quasi-periodic with less soliton energy variation. Further increasing the pump power, the same process as described above repeated. Quasi-periodic vector soliton intensity variations of multiple vector soliton in cavity were also observed. Figure 26 shows for example a case of two vector solitons coexist in the cavity. Each of the vector solitons

exhibits the quasi-periodic energy variation, as clearly shown in the oscilloscope trace. In the state the solitons in the cavity have uncorrelated intensity variation. No soliton energy quantization exists in the case. With too many vector solitons in cavity, the interaction among the solitons could become very complicated. Quasi-periodicity and quasi-periodic route to chaos is one of the intrinsic features of the nonlinear dynamic systems. This experimental results clearly show that the passively mode locked soliton fiber lasers are a nonlinear dynamic system that can be used as an ideal platform for the experimental study of the nonlinear dynamics.

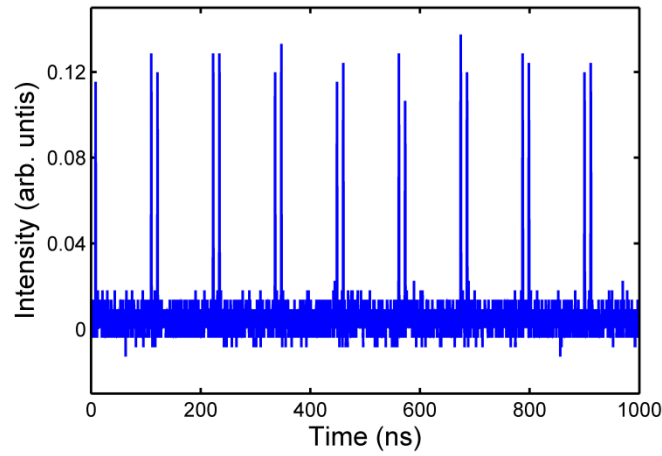


Figure 26: Oscilloscope trace of the laser emission under the quasi-periodic vector soliton intensity variation and with multiple vector soliton in cavity.

4.3 Graphene mode-locked Ytterbium-doped fibre lasers

Apart from mode locking the erbium doped fiber lasers, we have also used few layer graphene to mode lock the Yb-doped fiber (YDF) lasers. The YDF laser operates at $1.06 \mu\text{m}$, which is $\sim 500 \text{ nm}$ away from that of the erbium doped fiber lasers. Fig. 27 shows schematically the graphene mode locked Yb-fiber laser setup. A ring cavity configuration was adopted. The laser was bi-directionally pumped with two 975 nm pump lasers, to get large pump power. Each of the pump lasers has a maximum output power of 150 mW . A segment of 72 cm YDF with absorption of $1020 \text{ dB/m @ } 977 \text{ nm}$ (AD465-00 from FIBERCORE) was used as the gain medium. All the other fibers used were the standard SMF (Corning HI1060). A segment of around 210 m SMF was inserted

in the cavity to increase the cavity length so that a large energy mode locked pulse could be formed. The total cavity length was about 222 m. A fiber pigtailed polarization-independent isolator was used to force the unidirectional operation of the laser, and an inline polarization controller (PC) was used to fine tune the linear cavity birefringence.

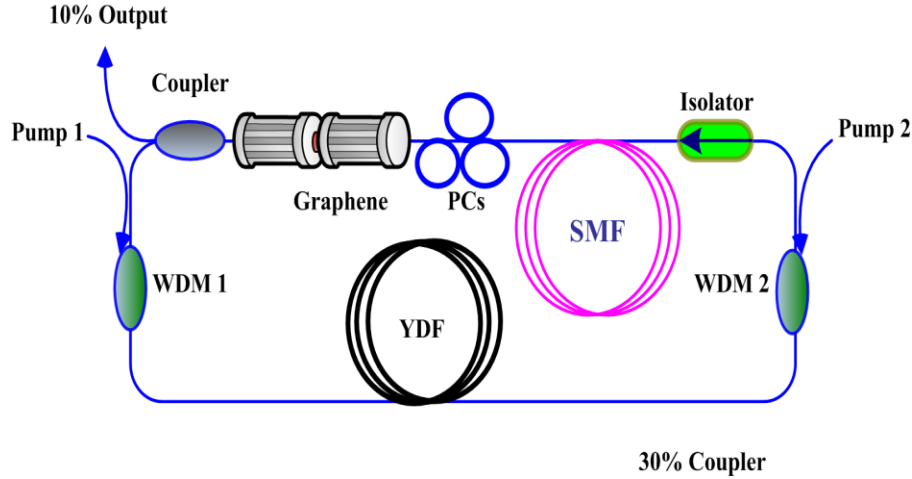


Figure 27: Schematic of the graphene mode locked Ytterbium-doped fiber laser. WDM: wavelength-division-multiplexer; YDF: Ytterbium-doped fiber; SMF: single mode fiber; PC: polarization controller.

It was found that with appropriate PC setting, self-started mode locking could occur in the laser at a pump power of 115 mW (with forward pump power of 60 mW and the backward pump power of 55 mW). Similar to the operation of the other passively mode locked fiber lasers, multiple pulses were initially obtained immediately after the laser mode locking. However, carefully reducing the pump power to 100 mW (with forward pump power reducing to 45 mW while maintaining the backward pump power of 55 mW), single pulse operation could be obtained as shown in Fig. 28. The optical spectrum, pulse train, pulse profile, and the RF spectrum of the mode locked pulses are shown in Fig. 28(a)-(d), respectively. The optical spectrum shown in Fig. 28(a) exhibits the characteristic steep spectral edges, which clearly shows that the mode locked pulses have been shaped to dissipative solitons, characterized by the sharp steep spectral edges of their optical spectrum. The central wavelength of the dissipative soliton is located at 1069.8 nm, and the 3-dB spectral bandwidth is about 1.29 nm. The optical pulses have a width of 580 ps, measured with a high-speed oscilloscope (Agilent 86100A) and a 45

GHz photodetector (New Focus 1014). The time-bandwidth-product therefore is 196, which shows that the dissipative solitons are strongly chirped, which is a typical feature of the dissipative solitons. The pulse train has a pulse repetition rate of 0.9 MHz. The signal-to-noise ratio of the fundamental repetition rate is larger than 70 dB above the noise level, indicating that the laser mode locking operation is very stable. The laser output power coupled through a 10% fiber coupler was about 0.37 mW. Therefore, the output pulse energy is about 0.41 nJ. The low peak power and broad pulse width of the generated dissipative soliton made it a perfect seed pulse source for pulse amplification.

The experimental result clearly demonstrated that graphene can also be used to mode lock the Yb-doped fiber lasers, despite of the fact that the Ytterbium doped fiber lasers operate at the wavelength of 1.06 μm , which is almost 500 nm away from the operating wavelength of the erbium-doped fibers. The experimental result confirmed that the graphene based saturable absorbers could have super broad wavelength-independent saturable absorption.

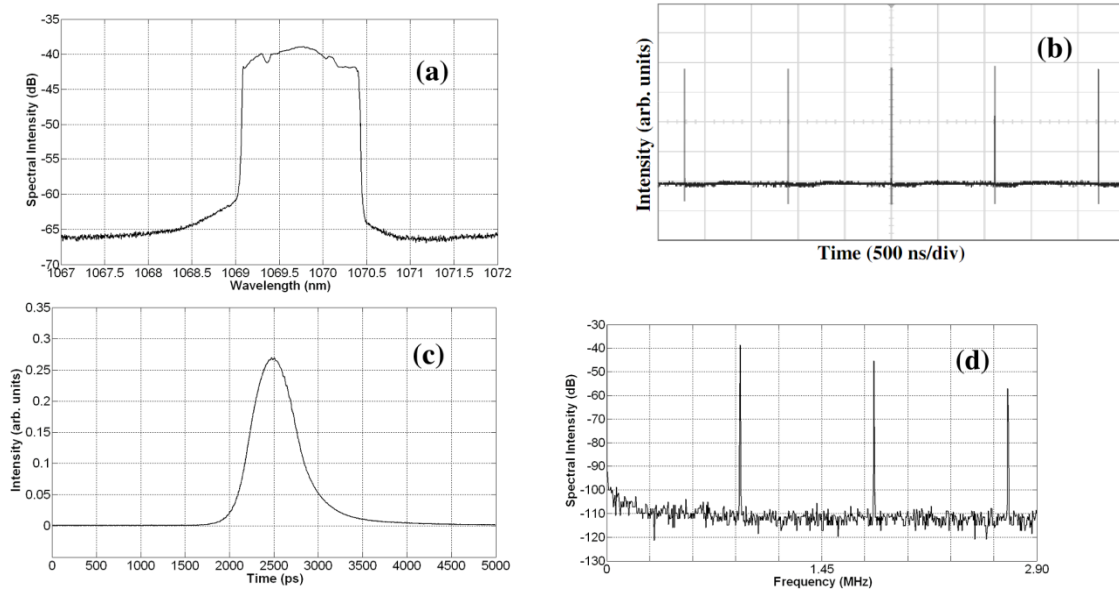


Figure 28: Operation of graphene mode-locked Yb fiber laser. (a) Optical spectrum, (b) pulse train, (c) pulse profile, and (d) RF spectrum of the mode locked pulses.

4.4 Graphene Q-switching and mode locking 2 μm solid state lasers

To further demonstrate the super broadband saturable absorption feature of the atomic layer graphene, and the feasibility of using graphene to mode lock lasers with different wavelengths, we also conducted experiments to study graphene mode locking of the Tm-doped solid state lasers. A schematic of the laser setup is shown in Fig. 29. A single-emitter laser diode at 790 nm was used as the pump source. The pump light was focused through two convex lens into a Tm:CLNGG crystal with a spot size of $26 \times 86 \mu\text{m}$. The Tm:CLNGG crystal employed in the experiment has a length of 9 mm and Tm-doping concentration of 3 at.% in melt. The crystal was placed at Brewster angle for minimizing the transmission loss for the p polarized light. To effectively remove the heat generated the crystal was wrapped with indium foil and tightly mounted in a water-cooled copper block. The circulating water temperature was set at 9.0°C . An X-folded cavity was employed to obtain a suitable laser mode size in the crystal and on the graphene SAM. Based on the ABCD matrix calculation, the laser mode has a radius of $\sim 35 \mu\text{m}$ in the crystal and $\sim 40 \mu\text{m}$ on the graphene SAM. The concave mirrors M1, M2, and M3 have a radius of curvature of 10 cm, and were highly reflectively coated at the laser wavelength and anti-reflectively coated at the pump wavelength. The wedged output coupler had a transmission of 2% at 2000 nm wavelength. In the experiment, a slit was inserted in the cavity to suppress the high-order transverse modes. A pair of CaF_2 prisms with a tip to tip distance of 40 cm was employed for intracavity dispersion compensation. The as-fabricated graphene SAM was used as passive Q-switching and mode-locking elements in the laser.

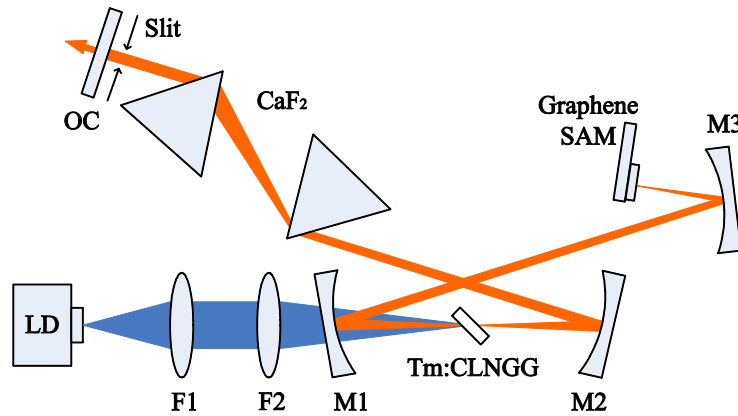


Figure 29: The schematic of the laser setup, LD: laser diode; F1, F2: convex lenses; M1, M2, M3: concave mirrors with same radius of curvature (ROC) of 10 cm; OC: output coupler; graphene SAM: graphene saturable absorber mirror.

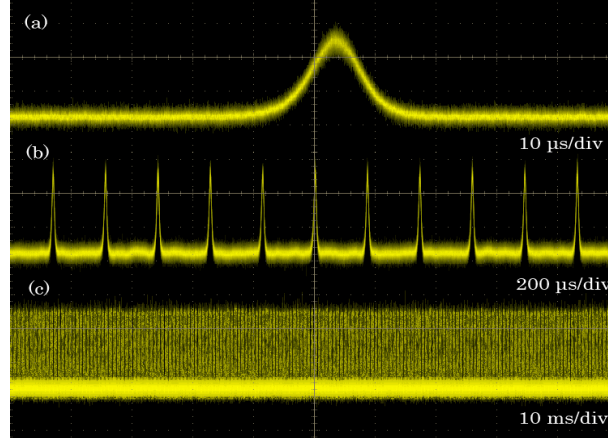


Figure 30: The Q-switched pulse trains in different time scales: (a) 10 $\mu\text{s}/\text{div}$; (b) 200 $\mu\text{s}/\text{div}$; (c) 10 ms/div .

Both the Q-switching and CW mode locking operations were obtained in the laser. The typical Q-switched pulse trains are shown in Fig. 30. The Q-switched pulses have a long pulse duration of 9 μs , which is attributed to the low modulation depth of the 1-2 layer graphene and long laser cavity used in the experiment. The Q-switched pulses have a repetition rate of 5.8 kHz. The average output power of the laser was 40 mW, thus the corresponding Q-switched pulse energy was 6.9 μJ . The Q-switched pulses were very stable and the pulse to pulse intensity fluctuation was estimated to be less than 5%. Fig. 31 shows the Q-switched pulse spectrum of the laser. The laser emission was centered at 2013.5 nm, with a narrow bandwidth of only ~ 1.2 nm.

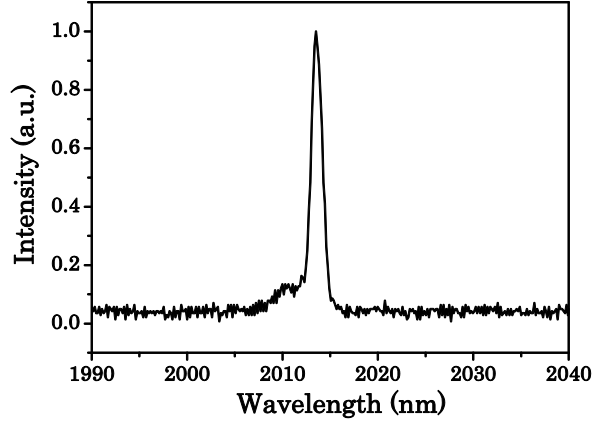


Figure 31: Spectrum of the Q-switched pulses.

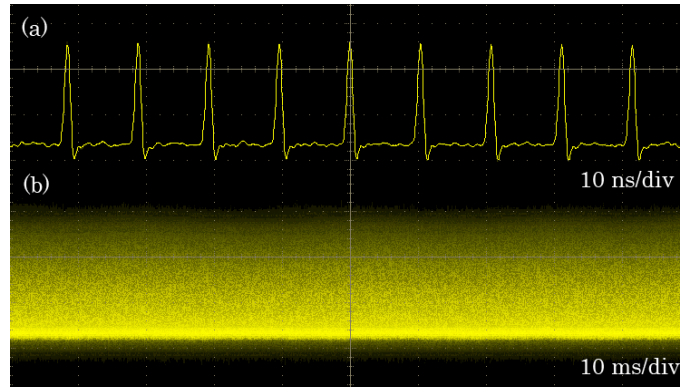


Figure 32: The CW mode-locked pulse trains in different time scales: (a) 10 ns/div; (b) 10 ms/div.

Stable CW mode locking was achieved in the laser through carefully optimizing the laser spot position on the graphene SAM and aligning the laser cavity. Fig. 32 shows a typical mode locked pulse train obtained. Under the mode locking the average output power of the laser increased to 60 mW at the same pump power. The mode-locked pulses had a repetition rate of 95 MHz, corresponding to the laser cavity length of 1.58 m. By checking the pulse trains in different time scales, no Q-switching envelope was observed, and the laser operated in CW mode locking.

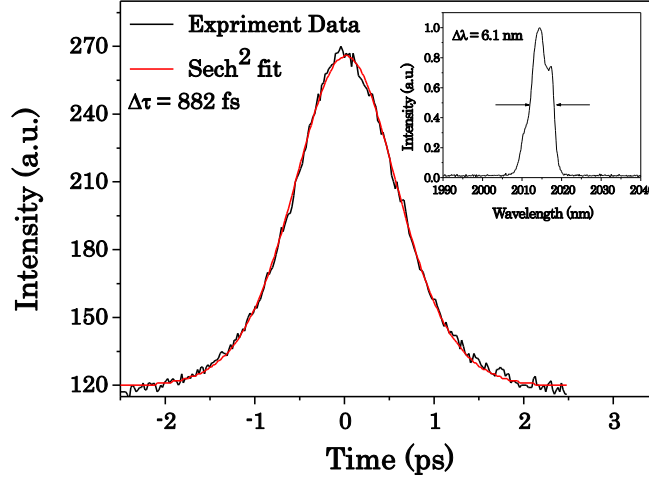


Figure 33: Autocorrelation trace of the mode locked pulses. Inset: the corresponding spectrum.

The autocorrelation trace of the mode locked pulses was measured with a commercial autocorrelator, as shown in Fig. 33. Assuming a Sech^2 shape, the mode-locked pulse duration was 882 fs. The spectrum of the mode locked pulses was measured using an optical spectrum analyzer with a resolution of 0.22 nm, shown in the inset of Fig. 33. The laser spectrum is centered at 2014.4 nm, with a bandwidth of 6.1 nm. The time-bandwidth product of the mode locked pulses is 0.39, close to Fourier transform limit value for Sech^2 -shape pulses.

To explain why both the Q-switching and mode locking could be obtained in the same laser under the same pump power, we believe it could be due to the non-uniformity of the graphene film. As shown in the graphene fabrication part, it is challenge to control the uniformity of the graphene film. It is possible the in some place it is a monolayer graphene, and in some other place it is bi-layer graphene, so depending on the positions used, the saturable absorption strength would be different, which could result in different operation of a laser.

5. Dark pulse emission of a semiconductor laser with delayed feedback

We had also conducted experiment to test the feasibility of using graphene to mode lock semiconductor lasers. We used a commercial quantum-well semiconductor laser operating at the wavelength of 770nm as it is available on hand. One facet of the

semiconductor laser is high reflection coated and the other one is anti-reflection coated. We had constructed an external cavity laser with a graphene saturable absorber mirror as the external cavity. Although we had used graphene with different number of layers, and saturable absorbers made of different graphene derivatives, no mode locking of the semiconductor laser was achieved. We suspect the reason could be that the operation wavelength of the semiconductor laser is too short. At the wavelength the saturation intensity of graphene could be too large. Based on our experience in working on the graphene mode locking of lasers, we found that the longer the laser operation wavelength, the easier to get the laser mode locked. Therefore, we stopped the experiment. We are currently in the process of purchasing another semiconductor laser module whose operation wavelength is at 1.45 μ m. We are going to continue the experiment once the new diode is available.

In the course of our experiment on the graphene mode locking of the 770nm semiconductor laser, we observed a novel form of dark pulse emission of the semiconductor laser under delayed feedback. We then focused our research to the effect of the laser. We used an experimental setup as depicted in Fig. 34. A quantum-well laser diode module operating at a solitary wavelength of $\lambda=770$ nm was used. One facet of the laser diode is high reflection coated, and the other one is anti-reflection coated. The laser diode was driven by an ultra-low noise current source (Sacher MLD-100) and mounted on a water-cooled copper block maintained at 17 °C. A wedge-shaped mirror M1 with a reflectivity of 30% was implemented as the external cavity mirror. To collimate the laser beam an antireflection-coated aspheric lens was set between the diode and the external cavity mirror. The laser output and its optical spectrum were simultaneously monitored by an optical spectrum analyzer with a resolution of 0.05 nm (Ando, AQ-6315B), and a 1 GHz bandwidth photodetector (NewFocus, 1611-FC-AC) together with a fast digital oscilloscope of the same bandwidth (Tektronix, DP0714). A photon detector (Gentec PH100-Si) was used to measure the output power.

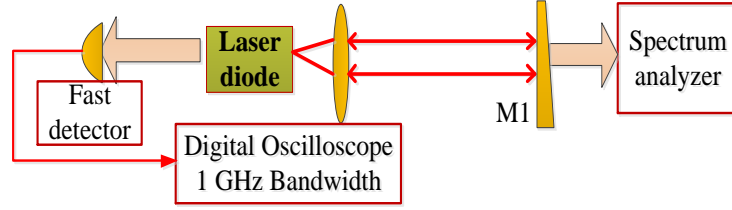


Figure 34: Schematic of the experimental setup

We first measured the operation of the laser diode under different injection currents with M1 was moved away, as shown in Fig. 35a and b, respectively. The diode started lasing as the injection current exceeded 80 mA, and its emission wavelength was at 770 nm. Under all the experimental accessible current range the diode emission was always in a CW mode. We then installed M1 as shown in Fig. 34. It was found that under the delayed feedback, the laser could exhibit different features. We had changed the external cavity length from 40cm to 170cm. At different external cavity lengths depending on the alignment of M1, CW emission of the laser could still be obtained. Fig. 35a shows for example the CW laser emission as the external cavity length was set as 37.5 cm. Under existence of the feedback the laser threshold decreased to 60 mA, and CW wavelength shifted to 781nm, while the slope efficiency of the laser is almost the same as that of the diode without feedback.

The CW emission was achieved under the optimized M1 alignment, corresponding to that the feedback has the strongest strength. Carefully misaligning M1, the laser then exhibited various emission features. Based on the laser oscillation wavelength we could easily identify the relative feedback strength. Under a relatively weak feedback, it was found that the laser was operating in the low frequency fluctuation (LFF) state, as shown in Fig. 36(a). Due to the irregular laser intensity drop-outs, the emission spectral bandwidth of the laser also obviously broadened, which was also called as the coherence collapse.

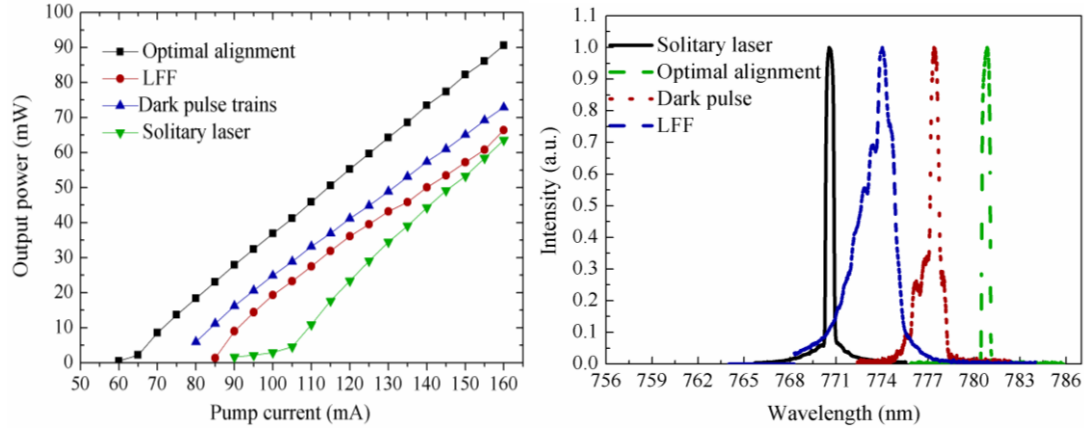


Figure 35: a) Characteristics of output power versus pump current. b) Spectra of laser diode in different regimes.

While as the optical feedback strength was increased, the drop-out events of the LFF became rare, with time intervals on the orders of ms, and eventually disappeared. Finally, the LFF evolved into a periodical dark pulse emission state, as shown in Fig. 37(a). The optical spectrum of the laser under the dark pulse emission is shown in Fig. 35b. Compared with that of the LFF emission, it is remarkably narrower. The output power of the laser under the dark pulse emission is depicted in Fig. 35b. It has a threshold injection current of 80 mA, which is a little bit higher than that of the CW laser emission. At the threshold of dark pulse operation, the laser output power is 6 mW. While increasing the injection current to 160 mA, the laser output power reached 73 mW.

Fig. 35b shows that as the feedback strength is increased, the central wavelength of the laser emission shifted to the longer wavelength, and the laser emission also evolved from LFF to stable dark pulse emission, and stable CW emission. The according spectral widths are about 0.56 nm, 1.97 nm, 0.61 nm and 0.55 nm, respectively. In the LFF regime, the spectral width is wider than the other regimes.

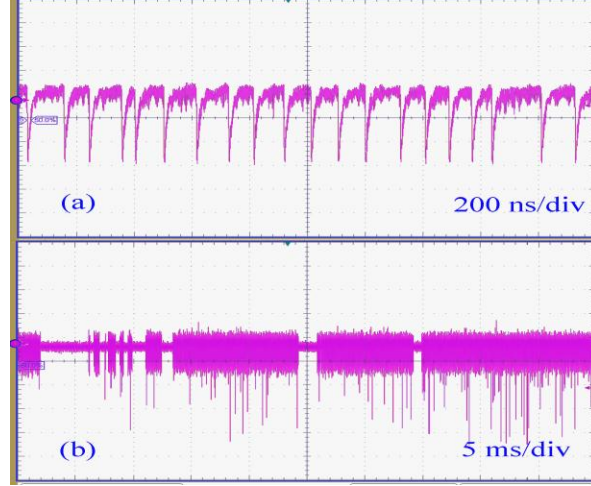


Figure 36: Dynamics of the semiconductor laser subject to optical feedback for $I=120$ mA, $L_{ext}=37.5$ cm. Experimental time traces of the LFF (a) and a transition from LFF to dark pulse state (b).

When the cavity length was about ~ 37.5 cm, the repetition rate of dark pulses was ~ 400 MHz (Fig. 37a). Seeing from Fig. 37b in time scale of 1 ms/div, the system worked in a stable state. While when the cavity length was increased to ~ 61 cm, the dark pulse repetition rate changed to ~ 244 MHz (Fig. 38a). The result clearly shows that there was one dark pulse within the cavity, and the dark pulse repetition rate varied with the cavity length. Depending on the details of the cavity alignment, multiple dark pulse emission was also observed. Fig. 38b shows a double pulse emission when the cavity length was ~ 61 cm. In fact, multiple dark pulse emission was much easier to obtain than the single dark pulse emission. A tiny adjustment of M1 could switch a single dark pulse emission state to a double dark pulse or multiple dark pulse emission state.

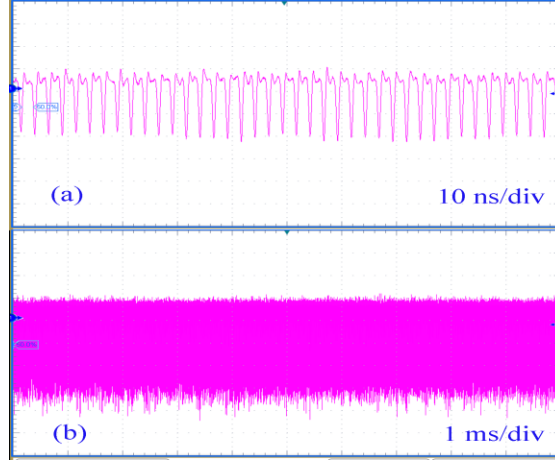


Figure 37: Intensity time series of single dark pulse trains for $I=120$ mA, $L_{ext}=37.5$ cm. (a) single dark pulse trains at a repetition rate of 400 MHz (b) stability of the dark pulse trains in a time scale of 1 ms/div.

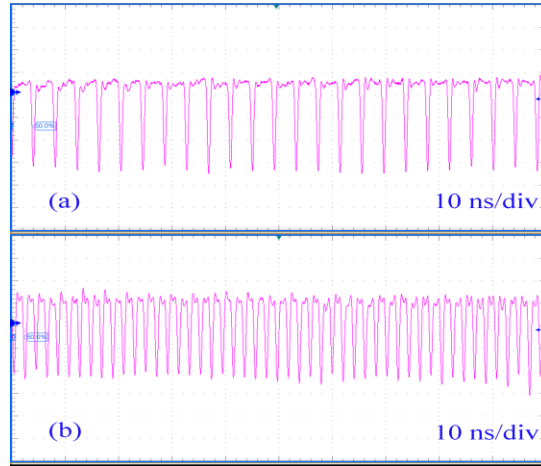


Figure 38: Intensity time series of dark pulse trains for $I=120$ mA, $L_{ext}=61$ cm. (a) single dark pulse trains at a repetition rate of 244 MHz. (b) multiple dark pulse trains at a repetition rate of 488 MHz.

The photodetector used in our experiment has AC coupling. Hence the actual darkness of the pulses could not be detected. To check the ratio of the dark pulse with the CW level, we further used a slower photodetector (NewFocus-1801-DC) with a bandwidth of 125 MHz to observe the modulation depth of the dark pulse trains. Considering the bandwidth of the photodetector, the length of the external cavity was extended to 170 cm, corresponding to the repetition frequency of 88 MHz. It shows a

modulation depth of about 35 %. Tested with a femto-second mode-locked laser source, we confirmed that our detection system (photodetector and oscilloscope) has a rising and falling time of ~ 400 ps, respectively. The measured FWHM width of the dark pulses was ~ 450 ps and they did not change with the experimental conditions, indicating that it is limited by our detection system. The actual dark pulse width should be narrower than 450 ps.

We note that stable dark pulse emission was also observed in a quantum dot (QD) semiconductor laser with a SESAM in cavity by Feng et al. However, in our laser cavity there is no saturable absorber or equivalent component. Therefore, no mode locking is possible. Carroll et al. also reported stable dark pulse emission from a QD laser induced by the optical feedback from a distance reflector. Our results resemble their results. However, it was considered that dark pulse is difficult to obtain in QW laser diodes and dark pulse dynamics is unique to the QD lasers. With appropriate amount of optical feedback, periodical dark pulses were also observed in our QW semiconductor laser. We speculate that there are two reasons for not observing the dark pulses in the past experiment. First, thanks to the progress of the semiconductor laser technology, the stability of laser diode has been greatly improved, which benefits to avoid the unwanted fluctuations to influence the dark pulse. Second, the anti-coating technique of the laser diode facets can reach 2% and even less, which can reduce the multiple reflections in the cavity.

To understand the stable dark pulse emission of the laser, we note that recently Zhang et al. reported the experimental observation of stable dark pulses in an erbium-doped fiber laser. It was shown whenever a bi-stable nonlinear system subject to delayed feedback could display dark pulse emission. The dark pulses were explained as a kind of dark soliton. Zhang et al.'s results remind us that the dark pulse emission could be a general feature of the delayed nonlinear feedback system, as under appropriate conditions its dynamics is governed by the CGLE. Therefore, we speculate that the observed stable dark pulses could be a kind of the dissipative dark cavity solitons formed in the laser. The hypothesis is also justified by the property of the dark pulses. Experimentally it was observed that as the feedback strength is increased, it also experienced pulse splitting.

6. Conclusions

In summary, using the CVD method we have fabricated high quality large size atomic layer graphene, and experimentally investigated graphene's nonlinear optical saturable absorption property. Our experimental results confirmed that the atomic layer graphene can exhibit ultrafast, super broadband, polarization insensitive saturable absorption, which can be exploited for the passive mode locking of lasers with various operating wavelength. Using atomic layer graphene as saturable absorber we have further successfully demonstrated the self-started mode locking of the erbium-doped fiber lasers operating at the 1.55 μm , the Yb-doped fiber laser operating at the 1.03 μm , and the Tm-doped solid state lasers operating at 2014nm. Through our experiments we found that the longer the laser operating wavelength, the easier to achieve the mode locking of a laser. Our experimental results clearly show that the atomic graphene is an excellent laser mode locker for lasers with wavelength longer than 1.0 μm , and the longer the laser operating wavelength, the better is its mode locking effect. To modify the saturable absorption property of graphene, especially to make the graphene mode locker more user friendly, we have also fabricated various graphene derivatives through chemical functionalization. Saturable absorption properties of the graphene derivatives were also experimentally investigated. Feasibility of some of the graphene derivatives for the passive mode locking of the erbium-doped fiber lasers was confirmed.

However, our attempt of using graphene to mode lock a semiconductor laser operating at 770nm failed. Currently we are investigating the physical reason. Based on the energy band structure of the graphene, the higher the photon energy the larger the saturation energy of the graphene is. We believe it may be due to this feature of the graphene, it is difficult to get the semiconductor laser to be mode locked.

As the future development of the project, we are going to continue the experiment on the graphene mode locking of semiconductor lasers, but with diode lasers with longer wavelength. In addition, it will be interesting to examine other nonlinear optical properties of the graphene, e.g. the optical Kerr effect, and the nonlinear wave mixing effects. Using graphene to mode lock long wavelength mid-infrared lasers, like the CO and CO₂ laser would also be interesting and is worth being studied.

7. Publications generated from the project

1. Y. F. Song, H. Zhang, **D. Y. Tang**, D. Y. Shen, “Polarization rotation vector solitons in a graphene mode-locked fiber laser,” *Optics Express*, 20, 27283-27289(2012).
2. L. Li, C. W. Xu, **D. Y. Tang**, R. J. Knize, D. Y. Shen “Periodic dark pulse emission induced by delayed feedback in a quantum well semiconductor laser,” *AIP Advances*, accepted, 2012.
3. J. Ma, G. Q. Xie, P. Lv, W. L. Gao, P. Yuan, L. J. Qian, H. H. Yu, H. J. Zhang, J. Y. Wang, and **D. Y. Tang**, “Graphene mode locked femtosecond laser at 2 μ m wavelength,” *Optics Letters*, 37, 2085-2087(2012).
4. G. Q. Xie, J. Ma, P. Lv, W. L. Gao, P. Yuan, L. J. Qian, H. H. Yu, H. J. Zhang, J. Y. Wang, and **D. Y. Tang**, “Graphene saturable absorber for Q-switching and mode locking at 2 μ m wavelength,” *Optical Materials Express*, 2, 878-883(2012).

Invited paper.

5. C. W. Xu, **D. Y. Tang**, W. D. Tan, J. Zhang, and R. J. Knize, “Dark Pulse Emission from a 780nm Diode Laser With External Cavity Feedback,” *CLEO-Pacific Rim conference*, 28 Aug. - 01 Sept. 2011, Sydney, Australia.
6. **D. Y. Tang**, “Chaotic dynamics of a graphene mode locked vector soliton fiber laser,” *International Symposium on Physics and Applications of Laser Dynamics* 6-9 October 2012, Tainan, Taiwan. **Invited Talk.**
7. Y. F. Song, L. Li, H. Zhang, **D. Y. Tang**, D. Y. Shen,” Quasi-periodicity of vector solitons in a graphene mode-locked fiber laser,” *Submitted to Laser Physics Letters*, 2012.

8. Research collaborations resulted from the work

1. Research collaboration with Prof. Randall J. Knize, Laser and Optics Research Center, United State Air Force Academy, on graphene photonics, graphene mode locking of lasers.

2. Research collaboration with Prof. G. Q. Xie, Physics Department, Shanghai Jiaotong University, China, on the graphene mode locking of $2\mu\text{m}$ solid state lasers.